Tréhu, A.M., Bohrmann, G., Torres, M.E., and Colwell, F.S. (Eds.)
Proceedings of the Ocean Drilling Program, Scientific Results Volume 204

15. Microbial Methane Generation and Gas Transport in Shallow Sediments of an Accretionary Complex, Southern Hydrate Ridge (ODP Leg 204), Offshore Oregon, USA[1]

George E. Claypool,[2] Alexei V. Milkov,[3] Young-Joo Lee,[4] Marta E. Torres,[5] Walter S. Borowski,[6] and Hitoshi Tomaru[7]

[1]Claypool, G.E., Milkov, A.V., Lee, Y.-J., Torres, M.E., Borowski, W.S., and Tomaru, H., 2006. Microbial methane generation and gas transport in shallow sediments of an accretionary complex, southern Hydrate Ridge (ODP Leg 204), offshore Oregon, USA. *In* Tréhu, A.M., Bohrmann, G., Torres, M.E., and Colwell, F.S. (Eds.), *Proc. ODP, Sci. Results,* 204, 1–52 [Online]. Available from World Wide Web: <http://www-odp.tamu.edu/publications/204_SR/VOLUME/CHAPTERS/113.PDF>. [Cited YYYY-MM-DD]
[2]8910 West Second Avenue, Lakewood CO 80226, USA. geclaypool@aol.com
[3]BP America, Exploration and Production Technology Group, Houston TX 77079, USA.
[4]Korea Institute of Geoscience and Mineral Resources, Daejeon 305-350, Korea.
[5]College of Atmospheric and Ocean Science, Oregon State University, 104 Ocean Administration Building, Corvallis OR 97331-5503, USA.
[6]Department of Earth Sciences, Eastern Kentucky University, 512 Lancaster Avenue, Richmond KY 40475-3102, USA.
[7]Department of Earth and Environmental Sciences, 227 Hutchison Hall, University of Rochester, Rochester NY 14627, USA.

Initial receipt: 1 February 2005
Acceptance: 1 March 2006
Web publication: 18 August 2006
Ms 204SR-113

ABSTRACT

Sediments at the southern summit of Hydrate Ridge display two distinct modes of gas hydrate occurrence. The dominant mode is associated with active venting of gas exsolved from the accretionary prism and leads to high concentrations (15%–40% of pore space) of gas hydrate in seafloor or near-surface sediments at and around the topographic summit of southern Hydrate Ridge. These near-surface gas hydrates are mainly composed of previously buried microbial methane but also contain a significant (10%–15%) component of thermogenic hydrocarbons and are overprinted with microbial methane currently being generated in shallow sediments. Focused migration pathways with high gas saturation (>65%) abutting the base of gas hydrate stability create phase equilibrium conditions that permit the flow of a gas phase through the gas hydrate stability zone. Gas seepage at the summit supports rapid growth of gas hydrates and vigorous anaerobic methane oxidation.

The other mode of gas hydrate occurs in slope basins and on the saddle north of the southern summit and consists of lower average concentrations (0.5%–5%) at greater depths (30–200 meters below seafloor [mbsf]) resulting from the buildup of in situ–generated dissolved micro-

bial methane that reaches saturation levels with respect to gas hydrate stability at 30–50 mbsf. Net rates of sulfate reduction in the slope basin and ridge saddle sites estimated from curve fitting of concentration gradients are 2–4 mmol/m^3/yr, and integrated net rates are 20–50 mmol/m^2/yr. Modeled microbial methane production rates are initially 1.5 mmol/m^3/yr in sediments just beneath the sulfate reduction zone but rapidly decrease to rates of <0.1 mmol/m^3/yr at depths >100 mbsf. Integrated net rates of methane production in sediments away from the southern summit of Hydrate Ridge are 25–80 mmol/m^2/yr. Anaerobic methane oxidation is minor or absent in cored sediments away from the summit of southern Hydrate Ridge.

Ethane-enriched Structure I gas hydrate solids are buried more rapidly than ethane-depleted dissolved gas in the pore water because of advection from compaction. With subsidence beneath the gas hydrate stability zone, the ethane (mainly of low-temperature thermogenic origin) is released back to the dissolved gas-free gas phases and produces a discontinuous decrease in the C_1/C_2 vs. depth trend. These ethane fractionation effects may be useful to recognize and estimate levels of gas hydrate occurrence in marine sediments.

INTRODUCTION

Leg 204 was dedicated to coring and logging the gas hydrate stability zone (GHSZ) within a 2 km × 6 km three-dimensional (3-D) seismic grid across southern Hydrate Ridge, a topographic high in the accretionary complex of the Cascadia subduction zone, ~80 km west of Newport, Oregon (USA) (Fig. **F1**). Hydrate Ridge is an area where gas hydrate occurs at or near the seafloor, and methane is venting into the water column (Torres et al., 2002; Heeschen et al., 2003). A regional bottom-simulating reflector (BSR) suggests that gas hydrate is widespread (Tréhu et al., 1999). Nine sites were drilled during Leg 204, four sites (1245, 1246, 1244, and 1252) along a west–east transect north of the southern summit, four sites (1247, 1248, 1249, and 1250) on a north–south transect up to the summit of the ridge, and Site 1251 in a slope basin east of the ridge. Water depths ranged from 795 to 1210 meters below sea level (mbsl) (Table **T1**). A logging-while-drilling hole and multiple-cored holes of varying depths were drilled at each site except at Site 1252, where a single hole was cored. Presence of gas hydrate at all sites except 1252 was confirmed by physical recovery from cores, pressure core samples, chlorinity anomalies, low core temperatures, and sonic and resistivity log responses (Tréhu et al., 2004).

Closely spaced samples of gas and pore water were collected from cores at all sites. In addition, 30 samples collected with the pressure core sampler (PCS) were retrieved intact and quantitatively degassed (Milkov et al., 2003), enabling measurement of subsurface gas contents as well as chemical and isotopic characterization. Gas and water samples were chemically analyzed onboard and isotopically analyzed postcruise. The Leg 204 *Initial Reports* volume (Tréhu, Bohrmann, Rack, Torres, et al., 2003) presents shipboard results, and Milkov et al. (2005) discuss isotopic compositions of gases. This report integrates the gas and pore water chemical and isotopic compositions and uses these data to infer the origins of the gas. The main issues to be addressed are the rates and quantities of gas generated by local microbial processes vs. the quantities resulting from upward flow from deeper sediments. The different gas supply processes affect the rate and magnitude of gas hydrate

F1. Leg 204 sites, p. 25.

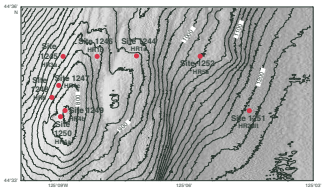

T1. Leg 204 site data, p. 41.

formation and are reflected in differences in gas hydrate occurrence on the accretionary ridge and in the slope basin. Compositionally distinctive gas migrating from depth is localized and defines the main migration pathways. In addition, gas hydrate formation imposes previously unrecognized fractionation effects on the gas geochemistry, which may be used to infer gas hydrate occurrence in other areas (Milkov et al., 2004a).

GEOLOGIC SETTING

Hydrate Ridge is a topographic high in the accretionary complex of the Cascadia subduction zone, ~80 km west of Newport, Oregon (Fig. F1). BSRs consistent with pressure and temperature conditions of methane hydrate decomposition occur throughout the region (Hyndman and Spence, 1992; Tréhu et al., 1999). Hydrate Ridge features two topographic summits, northern and southern, separated by a saddle. Site locations, water depths, BSR depths, and sediment accumulation rates are listed in Table T1. Previous coring (Ocean Drilling Program [ODP] Leg 146 Site 892) on northern Hydrate Ridge recovered gas hydrate at 2–19 meters below seafloor (mbsf), apparently related to a fault conduit containing migrated gas with a thermogenic component (Kastner et al., 1998; Hovland et al., 1995). Previous studies of Hydrate Ridge have documented the presence near both summits of seafloor gas vents, outcrops of massive gas hydrate, authigenic carbonates, and chemosynthetic communities (Suess et al., 1999; Torres et al., 2002; Boetius and Suess, 2004). Leg 204 objectives were to investigate the distribution and concentration of gas hydrates on southern Hydrate Ridge and in the adjacent slope basin and to evaluate the mechanisms that generate and transport methane and other gases into the GHSZ.

Subduction on the Oregon margin caused by convergence between the Juan de Fuca and North American plates occurs at a rate of ~400 km/m.y. (MacKay et al., 1992). Hydrate Ridge is the second accretionary ridge, ~20 km landward of the frontal thrust that marks the seaward edge of the accretionary prism. Allowing for some shortening associated with folding and faulting, this distance and convergence rate suggest that ~100 k.y. ago, sediments under Hydrate Ridge were being deposited on the outer edge of the Astoria Fan in water depths of 3 km. Since that time, Hydrate Ridge sediments have been tectonically uplifted to water depths of ~0.8 km, while accumulating only ~10–60 m of additional sediment (at biostratigraphic sedimentation rates of 100–600 m/m.y.) (Tréhu, Bohrmann, Rack, Torres, et al., 2003). This change in water depth has lowered hydrostatic pressure at the seafloor from 30 to 8 MPa and decreased the methane concentration requirement for hydrate stabilization at the base of hydrate stability by half, from ~180 to 90 mM dissolved CH_4. Superimposed on the large pressure decrease associated with tectonic uplift is a smaller pressure change (±0.12 MPa) associated with glacial–interglacial sea level changes of 120 m during the last 100 k.y.

Sediments at the outer edge of the Astoria Fan were cored at Site 174 during Leg 18 of the Deep Sea Drilling Project (DSDP) and are known to be gas-charged (Claypool and Kaplan, 1974), although the inferred methane contents at Site 174 are probably below solubility limits required for gas hydrate stabilization. Similar sediments originally deposited in deep water that have undergone pressure reduction associated with subduction thrust faulting and tectonic uplift could have liberated

a gas phase that would be free to find or create permeable channels and undergo buoyant migration toward the seafloor. Gas in excess of solubility would be available to form gas hydrates within the GHSZ, which would have thinned from ~400 to 120 m thick during uplift.

SAMPLES AND ANALYTICAL PROCEDURES

Four types of gas samples were collected during Leg 204: void gas, headspace gas, gas hydrate, and pressure core. Gas voids formed in the core liner were sampled by means of a core liner penetration tool with a 60-cm³ plastic syringe attached by a three-way stopcock. After sectioning the core, nominal 5-cm³ plugs of sediment collected using cut-off syringes or a cork borer were outgassed in vials and the headspace gases analyzed according to standard ODP procedures (Pimmel and Claypool, 2001). Small pieces of gas hydrate recovered from cores were quickly cleaned, placed in 60-cm³ syringes and allowed to decompose. Aliquots of gas samples collected during prolonged degassing of PCS cores were also collected in syringes. After shipboard gas chromatographic analysis, aliquots of all except headspace gas were saved for shore-based analysis by injecting into septum-sealed evacuated containers. Headspace methane results were used to estimate dissolved methane content of shallow samples. Procedures for sampling and analysis of pore waters are detailed in the "Explanatory Notes" chapter of the Leg 204 *Initial Reports* volume (Shipboard Scientific Party, 2003a).

Isotopic analyses were performed at Woods Hole Oceanographic Institution (USA), and the detailed analytical procedures are given in Milkov et al. (2005). The carbon isotopic composition of the dissolved inorganic carbon from interstitial water samples was analyzed at Oregon State University (USA). Water samples were acidified with phosphoric acid in an online preparation system and the evolved CO_2 measured on a mass spectrometer.

RESULTS

Chemical Composition of Gas

The results of the shipboard gas chromatographic analyses of gas samples are presented in the individual site chapters of the Leg 204 *Initial Reports* volume (Tréhu, Bohrmann, Rack, Torres, et al., 2003). Figure F2 summarizes the chemical composition of gases in terms of the C_1/C_2 ratio. Four general patterns of C_1/C_2 composition are illustrated by the different sites cored during Leg 204. At Sites 1245 and 1247 the C_1/C_2 values are high (10^5–10^4) in the uppermost 100–120 m beneath the seafloor then decrease rapidly to low values (10^2) at depths corresponding to the occurrence of seismic Horizon A (150–175 mbsf), a high-amplitude feature found in cores to be an ash/turbidite layer. Sites 1244, 1246, and 1251 are on the landward (east) side of Hydrate Ridge and are not underlain by Horizon A. These sites show a significant offset in C_1/C_2 values at the base of gas hydrate stability, from high to intermediate (10^3) values. Site 1252 is in a similar landward position with respect to the ridge but shows a gradual decrease in C_1/C_2. Sites 1248, 1249, and 1250 at or near the summit of Hydrate Ridge show a pattern inverse to that typically found in ODP cores in that C_1/C_2 values are low to inter-

F2. Void gas C_1/C_2 ratios, p. 26.

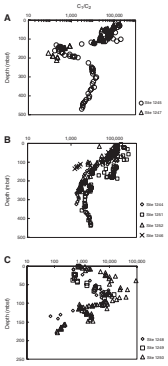

mediate near the seafloor and increase to high values at 50–100 mbsf. With further increase in depth at Sites 1248 and 1252 the C_1/C_2 values decrease again toward the BSR and Horizon A.

Isotopic Composition of Gas

Table T2 lists $\delta^{13}C$ values of CH_4 and CO_2 in void gas samples, and Figure F3 illustrates the variation in $\delta^{13}C$ of CH_4 as a function of depth of burial, which shows patterns similar to those observed for C_1/C_2 ratios. That is, Sites 1245 and 1247 show the heaviest (least negative) $\delta^{13}C_1$ values at the depth of seismic Horizon A. Sites 1244, 1246, 1251, and 1252 show more or less monotonic increases in $\delta^{13}C_1$ with increasing depth of burial. Sites 1248, 1249, and 1250 show heavy $\delta^{13}C_1$ values at or near the seafloor and become lighter with increasing depth to ~80 mbsf, and then become heavy again. The $\delta^{13}C$ values of CO_2 are not plotted but are generally subparallel with the $\delta^{13}C_1$ values.

Table T3 gives $\delta^{13}C$ values of C_2–C_5 hydrocarbon components in void gas samples that contained elevated amounts of higher hydrocarbons. Most of the measured $\delta^{13}C$ values for C_3–C_5 hydrocarbons are isotopically heavy (from –27‰ to –23‰) compared with the $\delta^{13}C_1$ values. However, the $\delta^{13}C$ values of ethane appear to represent different populations, as shown in the plot of C_1/C_2 vs. $\delta^{13}C_2$ (Fig. F4). Ethane components in gas samples with relatively low C_1/C_2 ratios have isotopically heavy values (from –32‰ to –28‰), whereas ethane in samples with high C_1/C_2 values is light (from –54‰ to –44‰).

Table T4 gives the δD values of CH_4 in selected void gas samples. The δD values of methane range from –208‰ to –187‰, are generally parallel to $\delta^{13}C$ values, and are in the same range observed for δD when measured in other DSDP/ODP cores.

The $\delta^{13}C$ values of CH_4 in gas samples from the PCS cores are listed in Table T5 and plotted vs. depth in Figure F5. The methane given off during the PCS degassing experiments had $\delta^{13}C$ values that were consistent with those of void gas samples at the nearby depths. Gas collected in multiple aliquots showed random variations of ±1‰.

The isotopic compositions of gases liberated from gas hydrate samples collected during Leg 204 are presented in Table T6. More complete discussion of the chemical and isotopic compositions of gas hydrate–bound gases and their relation to void gases is given in Milkov et al. (2005).

Isotopic Composition of Dissolved Inorganic Carbon

Table T7 presents the $\delta^{13}C$ values of dissolved inorganic carbon (DIC), present in the subsurface mainly as bicarbonate ion (HCO_3^-). Figure F6 is a plot of the $\delta^{13}C$ of DIC in pore water samples from 0 to 50 mbsf at Sites 1244, 1245, 1246, 1247, 1251, and 1252. All of these sites show a similar pattern, with seawater values (assumed $\delta^{13}C$ of ~0 ‰) at the seafloor decreasing to minimum values from –23‰ to –18‰, except for Sites 1245 and 1246, which have minimum values of –25‰ and –30‰, respectively. The depth of the minimum in the $\delta^{13}C$-DIC curve corresponds exactly with the depth at which dissolved sulfate is depleted, as discussed below.

Values for $\delta^{13}C$-DIC in pore water samples from Sites 1248, 1249, and 1250 at and near the summit are not plotted, but are all ^{13}C-enriched

T2. Void gas C_1 and C_2 isotope composition, p. 42.

F3. Void gas methane $\delta^{13}C$, p. 27.

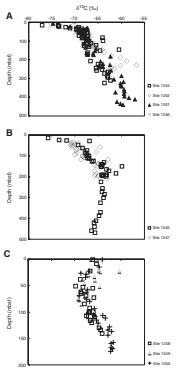

T3. Void gas C_2–C_5 isotope composition, p. 45.

F4. Ethane $\delta^{13}C$ composition, p. 28.

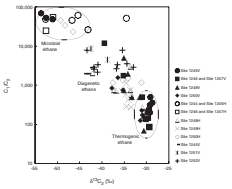

T4. Void gas methane δD, p. 46.

T5. PCS gas C_1 and C_2 isotope composition, p. 47.

F5. Methane $\delta^{13}C$ composition, p. 29.

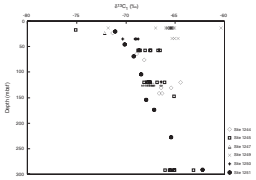

T6. Gas hydrate–bound C_1 and C_2 isotope composition, p. 48.

T7. DIC carbon isotope, p. 49.

(from +13‰ to +17‰), except for three samples from interval 0–1.4 mbsf at Site 1248 that have negative $\delta^{13}C$ values (from –24‰ to –1‰).

Leg 204 pore water analyses are presented in the individual site chapters of the Leg 204 *Initial Reports* volume (Tréhu, Bohrmann, Rack, Torres, et al., 2003). These results provide the framework for the following discussion of diagenetic processes occurring in the shallow sediments at Hydrate Ridge. The main results discussed are concentration-depth profiles of dissolved sulfate, alkalinity (bicarbonate), calcium, magnesium, ammonium, and phosphate.

F6. DIC $\delta^{13}C$ composition, p. 30.

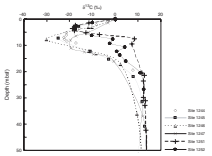

DISCUSSION

Chemical Composition of Interstitial Waters

Natural gas geochemistry at southern Hydrate Ridge is complicated by gas migrating from depth and mixing with gas generated in the shallow sediments. Gas samples with the migrated gas component were recovered in shallow sediments at Sites 1248, 1249, and 1250 and in sediments in and near Horizon A at Sites 1245 and 1247. The slope basin sites (1244, 1251, and 1252) and ridge saddle sites (1245, 1246, and 1247) at shallow depths represent sediments dominated by microbial methane generated during early diagenesis. Gas hydrate concentrations are much higher at the summit sites compared with sites away from the summit (20% of pore volume compared with 2%–5% of pore volume), indicating the importance of gas transport for sustaining higher concentrations of gas hydrate in surface sediments. Gas hydrates at nonsummit sites do not form until organic matter remineralization and microbial methanogenesis builds dissolved methane concentrations to hydrate solubility levels. Thus, there are two contrasting styles of gas hydrate formation at south Hydrate Ridge, here termed "transport-dominated" and "reaction-dominated" gas hydrate systems.

Transport-Dominated Gas Hydrate

One of the most important results of Leg 204 was determining the gas geochemistry, which defines the dominant migration pathways for gas from depth to the seafloor and results in venting of gas and formation of gas hydrate in surface sediments (Milkov et al., 2005). The pathways are localized in the summit region first by Horizon A, a northeast-dipping high-amplitude reflector shown by coring and logging to contain methane-rich gas at high gas saturation levels (40%–80%) with a significant component of C_2–C_5 hydrocarbons of deeper, thermogenic origin; second by the intersection of Horizon A with the base of the GHSZ; third by migration of gas through vertical gas chimneys above these intersections to the seafloor and near-surface sediments; and then laterally up to the topographic summit. These migration pathways are traced by means of the distinctive gas geochemistry, mainly the isotopically heavy C_2–C_5 hydrocarbons. However, the methane component of the total gas stream is isotopically light methane ($\delta^{13}C_1$; from –65‰ to –62‰) of apparent microbial origin. The methane component of the gas must be dominated by previously generated microbial methane buried with sediments of the accretionary prism that is now migrating along permeable pathways back to the seafloor, and carrying with it a minor component of thermogenic gas.

Proportions of Gas Sources

At the summit of Hydrate Ridge, the gas appears to result from three sources: (1) a minor thermogenic source characterized by a full suite of isotopically heavier C_2–C_5 hydrocarbons, (2) microbial methane that was buried with and then exsolved from accreted sediments, and (3) microbial methane currently being generated at shallow depths of burial. The relative proportions of these three sources can be roughly estimated. The fact that there is three or four times as much gas hydrate at the summit sites as there is at the nonsummit sites (Tréhu et al., 2004), where only normal microbial processes are operating, suggests that the exsolved and migrated microbial methane plus thermogenic component is ~75%–80% of the gas at the summit. The proportion of this migrated component made up by thermogenic gas can be estimated from the chemical and isotopic composition. The $\delta^{13}C$ of C_2–C_5 components can be used to infer that the $\delta^{13}C$ of thermogenic methane is about –45‰, according to the method outlined by Chung et al. (1988) and illustrated in Figure F7. If the end-member composition of the thermogenic component, in terms of $\delta^{13}C$ of methane and C_1/C_2 ratio, is –45‰ and 10, and for the microbial component is –68‰ and 10,000, then simple two-component mixing models suggest that the proportion of thermogenic gas in the migrated hydrocarbon stream is ~20%–25%. This means the relative proportions of the three source components at the summit sites would be ~20% microbial methane generated in the surface sediments, 65% microbial methane venting from accretionary prism sediments, and 15% thermogenic gas migrating from depth. The isotopic composition of the thermogenic gas suggests origin at temperatures of 125°–135°C, or depths of 2–2.2 km (Rooney et al., 1995).

F7. Estimation of thermogenic end-member, p. 31.

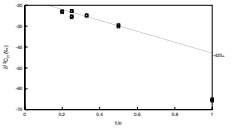

Gas Transport through the Gas Hydrate Stability Zone

It is frequently proposed that a critically pressured free gas column can build up beneath a seal created by the base of gas hydrate stability (de Boer et al., 1985; Grauls, 2001; Hornbach et al., 2004; Flemings et al., 2003). This situation, however, would seem to be inconsistent with the concept of the base of gas hydrate stability being a pressure-temperature (P-T) equilibrium surface. If gas pressure builds up and excess water is present, then gas should react with water to form additional gas hydrate until the pressure is brought back to equilibrium for the prevailing temperature. The presence of free gas at high concentration in a confined migration pathway may reconcile this apparent contradiction.

At several Leg 204 sites where the ash/turbidite layer (Horizon A) was drilled and logged beneath the GHSZ, there was evidence for gas saturation 40%–80% of porosity (Tréhu, Bohrmann, Rack, Torres, et al., 2003). As discussed earlier, the gas in Horizon A has a characteristic chemical and isotopic composition that enables delineation of migration pathways. It appears that free gas is migrating through Horizon A to the base of the GHSZ, then through vertical seismic features (gas chimneys) to the seafloor. Estimated P-T conditions at the base of the GHSZ beneath southern Hydrate Ridge are 9.6 MPa and 11.3°C. Under these conditions (methane compressibility factor [z] = 0.85), porous rocks containing 65 vol% CH_4 and 35 vol% water would have a CH_4-H_2O system composition of 14.4 mol%, equivalent to the formula $CH_4 \cdot 5¾H_2O$. This suggests that when a gas stream migrates in the presence of <35% water

saturation at these P-T conditions and moves into the GHSZ, available water converts to gas hydrate and a liquid phase, at least locally, would not be present. This creates conditions under which free gas and gas hydrate can coexist within the GHSZ. Moreover, it is an implication of the phase rule (number of components + 2 – number of phases = degrees of freedom) that the system gains an additional degree of freedom because of localized loss of the liquid phase so that gas pressure can rise above hydrostatic. In this view, system composition (high gas saturation at the base of the GHSZ) is the primary factor that allows both the existence of free gas and some degree of gas overpressure to occur at the base of and within the GHSZ.

High salinities created when salt is excluded during gas hydrate formation (Torres et al., 2004) can also stabilize free gas at shallow depths within the GHSZ (Milkov et al., 2004b). There is no evidence, however, for high salinity at the base of gas hydrate stability or in the vertical gas chimneys as sampled at Site 1248.

Double Bottom-Simulating Reflector

Leg 204 seismic data show the presence of a faint, deeper, second BSR on the seaward side of southern Hydrate Ridge in places where Horizon A underlies the prominent regional BSR. This second BSR is imaged and noted in illustrations from the Leg 204 *Initial Reports* volume chapters for Site 1245 (fig. F3; Shipboard Scientific Party, 2003b), Site 1247 (fig. F3; Shipboard Scientific Party, 2003c), and Site 1248 (fig. F3; Shipboard Scientific Party, 2003d). The estimated depths, temperatures, and hydrostatic pressures at the upper (BSR_1) and lower (BSR_2) reflectors near the site locations are given in Table **T8,** along with the calculated gas hydrate decomposition temperatures for two different gas mixtures. The gas mixture used to calculate hydrate decomposition temperatures at BSR_1 is a three-component mixture with a C_1/C_2 ratio of ~3000 and traces (a few parts per million) of propane (normalized molar fraction = C_1:0.99961, C_2:0.00033, and C_3:0.00006). The gas mixture used to calculate BSR_2 hydrate decomposition temperatures is a six-component mixture with a C_1/C_2 ratio of ~200 and significant amounts of C_3–C_5 hydrocarbons (normalized molar fraction = C_1:0.9900, C_2:0.005, C_3:0.0025, *i*-C_4:0.001, *n*-C_4:0.001, and C_5:0.0005). The first gas mixture is relatively pure methane, similar to that found in void gas samples in cores just above BSR_1. The second is a wetter gas mixture characteristic of void gas in zones a few meters above and below Horizon A. Nonhydrocarbon gas components (O_2, N_2, and CO_2) were neglected because they are believed to be mainly artifacts of air contamination and dissolved bicarbonate decomposition.

The calculations summarized in Table **T8** show that the observed zonation of gas composition in Hydrate Ridge sediments is consistent with a GHSZ that is stable to greater depths and temperatures than relatively pure methane (Structure I) gas hydrate and with the occurrence of a second, deeper (Structure II) BSR. Obtaining these consistent results using the observed gas composition and the Colorado School of Mines Hydrate (CSMHYD; Sloan, 1998) computer program requires use of a uniform regional thermal gradient (58°C/km) that is the approximate mean of the corrected values measured at individual sites during Leg 204 (**Tréhu,** this volume).

Additional evidence for the existence of gas hydrate beneath the presumed Structure I gas hydrate BSR_1 is threefold. First, some void gas

T8. BSR temperature and depth, p. 50.

samples collected from depths beneath BSR_1 are highly enriched in propane, a possible consequence of voids that formed in the vicinity of decomposing Structure II gas hydrate. Examples are Sections 204-1245B-19X-3 and 204-1248C-15H-1. Structure II gas hydrates enclose gas that is significantly enriched in propane relative to the feed gas from which it was formed. These gas samples are present at depths near the computed depths of BSR_2, where propane selectively removed from dissolved gas within the hydrate stability zone would have been released upon gas hydrate decomposition. Second, some headspace gas samples collected beneath BSR_1 contained greater amounts of gas than would have been expected from residual dissolved gas. Examples are Sections 204-1245B-16X-4 and 204-1247B-22X-2. Third, some sediment samples collected beneath BSR_1 for headspace gas analysis in a 1-cm-diameter brass cork-boring tube appeared to freeze inside the tube between the time of collection and displacement from the tube (with some difficulty) by means of a wooden dowel. Freezing of the water in the sediment could have been due to heat taken up by decomposition of Structure II gas hydrate.

Reaction-Dominated Gas Hydrates

In contrast to Leg 204 sites with evidence for migrated hydrocarbons, the gas geochemistry of cored sediments at Sites 1244, 1246, 1251, and 1252 and of shallow sediments at Sites 1245 and 1247 does not show obvious influence of migrated hydrocarbons. These sites are characterized by relatively steep concentration gradients in the microbial metabolites (SO_4^{2-}, HCO_3^-, CH_4, NH_4^+, and PO_4^{3-}). Whereas diffusive flux obviously occurs, the gradients are primarily caused by rapid reactions driven by the decomposition of sedimentary organic matter. The gas hydrates that develop under these circumstances are referred to as reaction-dominated gas hydrates, in contrast with previously discussed transport-dominated gas hydrates.

Methane is generated in shallow anoxic sediments as part of the normal process of organic matter remineralization (Claypool and Kaplan, 1974). Microbial respiration processes are ubiquitous in sediments where an adequate supply of metabolizable organic matter is present. Respiration involves the transfer of electrons from chemically reduced substances to oxidized substances, with capture of some of the energy produced enabling continuation of life processes.

Microbial Redox Reactions

In the terminal stages of the complex process of organic matter remineralization in marine sediments, soluble intermediate compounds are fermented (anaerobically oxidized) according to the general reaction

$$2CH_2O(NH_3)_{0.15}(H_3PO_4)_{0.01} + 4H_2O \rightarrow$$
$$2HCO_3^- + 0.3NH_3 + 0.02H_3PO_4 + 8e^- + 10H^+,$$

shown here for organic matter with approximate Redfield stoichiometry. For each eight electrons produced, the main products of organic matter oxidation are 2 mol bicarbonate plus 0.3 mol ammonia and 20 mmol phosphate. This oxidation half-cell reaction only proceeds when coupled with electron removal (reduction) reactions. Aerobic respiration involves the reduction of oxygen:

$$2O_2 + 8e^- + 8H^+ \rightarrow 4H_2O.$$

In anoxic marine sediments, the main electron removal reactions are sulfate reduction,

$$SO_4^{2-} + 8e^- + 8H^+ \rightarrow HS^- + 3H_2O + OH^-,$$

and, after sulfate is exhausted, the reduction of carbon dioxide (or bicarbonate) to form methane,

$$HCO_3^- + 8e^- + 8H^+ \rightarrow CH_4 + 2H_2O + OH^-.$$

In addition, an important reaction for carbon mass balance is the reaction of carbonate ion (or bicarbonate) with dissolved calcium and magnesium to form authigenic carbonate:

$$HCO_3^- + (Ca, Mg)^{2+} \rightarrow (Ca, Mg)CO_3 + H^+.$$

Under certain conditions (high flux of methane into sulfate reduction zone), it is also possible for methane to be anaerobically oxidized:

$$CH_4 + 3H_2O \rightarrow HCO_3^- + 8e^- + 9H^+,$$

when coupled with sulfate reduction. Note that anaerobic oxidation of methane produces only 1 mol bicarbonate (and no ammonia or phosphate) for each eight electrons produced.

The progress of these reactions can be followed as concentration and stable isotope changes with increasing depth downcore in marine sediments. The main complicating factors include simultaneously occurring reactions and diffusive transport of reactants and products. A major effect of these processes is the transfer of material from the solid sediment (organic matter and iron oxides) and overlying ocean (SO_4^{2-}, Ca^{2+}, and Mg^{2+}) to the pore water and back to the solid sediment (as iron sulfides, authigenic carbonate, and methane hydrate). These transfers also involve some vertical redistribution of material as a result of the different burial rates of sediment and pore water induced by compaction.

Burial Velocities and Advection from Compaction

The water content of sediments generally decreases with increasing depth of burial because of compaction under the influence of gravity. In accretionary prisms, effects of horizontal forces can also enhance water loss. Compaction causes differences in the relative motion of the sediment grains and the entrained pore water, which has important consequences for early diagenetic reactions and formation of gas hydrates. Under normal circumstances, both sediment grains and pore water are being buried and moved downward relative to the upwardly moving seafloor or sediment/water interface. However, the sediment moves downward at a faster rate than the water, and viewed from the standpoint of a given sediment layer, pore water is being advected upward. One consequence of these differences in downward burial velocity is that pore water is older than the sediment layer containing it and has had a longer time for reactions to proceed than is indicated by the age of the sediment.

The methods to track the relative movements of sediments and pore water during compaction are outlined by Berner (1980). Although compaction and porosity reduction are continuous, the main loss of porosity occurs at shallow depths (uppermost 50–100 mbsf). Compared with porosity loss at shallow depth, compaction at depths greater than a few hundred meters can be considered negligible. Using these considerations, the burial velocities of sediment and pore water are

$$\omega = [(1 - \phi_x)/(1 - \phi)]\omega_x$$

and

$$\nu = (\phi_x/\phi)\omega_x,$$

where

- ω = burial velocity of sediment,
- ν = burial velocity of pore water,
- ϕ = porosity, and
- x = value of porosity and burial velocity at depths where further compaction is negligible.

The burial velocities indicate time spent in a given depth interval, which can be integrated with depth to provide age vs. depth functions for the sediment and pore water. Figure F8 shows the porosity vs. depth and age vs. depth relationships for Site 1251. Porosity vs. depth is reasonably well described by $\phi = 0.79x^{-0.06}$, and this equation is used to calculate the burial velocities as a function of depth. A value of 500 m/m.y. as the sediment burial velocity (ω_x) at depths where further porosity decrease is negligible enables matching of the sediment burial velocity with the independently determined biostratigraphic sedimentation rate (Tréhu, Bohrmann, Rack, Torres, et al., 2003). These differential burial velocities become important in calculating rates of diagenetic processes and understanding fractionation effects associated with transfer of material between the solid and aqueous or gaseous phases.

F8. Porosity and age, p. 32.

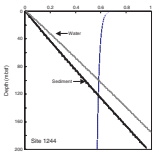

Sulfate Reduction and Evidence for Anaerobic Methane Oxidation

At sites near southern Hydrate Ridge but away from the summit, early diagenetic processes are best displayed by changes in pore water chemistry in sediments from the seafloor to ~50 mbsf. Sulfate concentration profiles for Sites 1244, 1245, 1246, 1247, 1251, and 1252 are shown in Figure F9. Sulfate gradients at summit Sites 1248, 1249, and 1250 could not be evaluated because sulfate was apparently depleted in the uppermost 15 cm of sediment beneath the seafloor (Boetius et al., 2000), a depth interval that is not well sampled in ODP operations. All of the sites away from the summit have similar shaped profiles, with sulfate concentrations greater than seawater frequently present in the upper 2–5 mbsf, then decreasing rapidly and approaching complete exhaustion at 5–12 mbsf. The dissolved sulfate profiles have an inverted S shape, being concave upward near the seafloor and concave downward at depths where sulfate approaches zero. The elevated sulfate concentrations near the seafloor suggest that some sulfide is being oxidized, possibly associated with bioirrigation or convective pumping of oxic

F9. Dissolved sulfate concentration, p. 33.

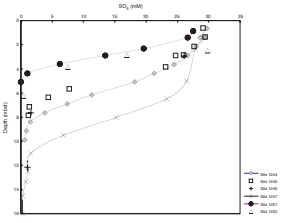

bottom water to ~2–5 mbsf. The nonsummit site closest to the summit (Site 1247) has the deepest apparent influx of sulfate-containing water, whereas sites farthest from the summit (Sites 1251 and 1252) have the shallowest.

Sulfate profiles appear to be sublinear over the midrange concentration intervals (20–5 mM) but concave downward over lower ranges (5–0 mM). These dissolved sulfate gradients can be used to estimate net rates of sulfate reduction. Net rates calculated from concentration profiles are gross rates minus the rate of reoxidation (Jørgensen et al., 2004). Net rates are generally less than rates measured by radiotracer techniques. The rate of sulfate reduction can also be estimated from the total flux of sulfate from the overlying ocean into the sediment, or the diffusive flux plus the burial flux. This flux is equivalent to the depth-integrated net sulfate reduction rate (SRR) per unit area (Canfield, 1991):

$$\text{Area SRR (mmol/m}^2\text{/yr)} = \phi_x D_s (dC/dx) + \phi_o \omega C_o,$$

where

ϕ_x = average porosity,
ϕ_o = initial porosity,
D_s = whole sediment diffusion coefficient for sulfate (average 6000 m²/m.y.),
dC/dx = sulfate concentration gradient (mmol/m⁴),
ω = estimated sedimentation rate (m/m.y.), and
C_o = initial sulfate concentration (29,000 mmol/m³).

The apparent linear sulfate concentration gradients can be used directly to give estimates of integrated sulfate reduction rates. The sulfate concentration profile also can be fit with an exponential function and rates interpreted in the context of steady-state diagenesis (Berner, 1980):

$$C = (C_o - C_\infty)\exp[-(k/\omega)x] + C_\infty,$$

where

k = first-order rate constant,
x = depth in meters beneath the zone of surface sulfate penetration,
C_o = initial sulfate concentration at the base of the bioirrigation or downwelling zone (29 mM) and,
C_∞ = projected asymptotic sulfate concentration where metabolizable organic matter would be exhausted.

In the case of Leg 204 nonsummit sites, C_∞ is a large negative number (e.g., –80 mM at Site 1244).

The rate of sulfate reduction within a given volume of sediment as a function of depth can be calculated from (Berner, 1980):

$$\text{Volumetric SRR (mmol/m}^3\text{/yr)} = 0.5 F k G_o \exp[(-k/\omega)x],$$

where

0.5= number of moles of sulfate reduced per mole of organic matter oxidized,

F = factor converting sediment from mass to volume concentration units (average = 1,400,000 g/m^3), and
G_o = concentration of metabolizable organic matter (mmol/g) calculated from (Berner, 1980),

$$G_o = [(C_o - C_\infty)(\omega^2 + kD_s)]/\omega^2 0.5F.$$

Volumetric rates of sulfate reduction as a function of depth can be integrated over the depth interval where sulfate reduction takes place and compared with the integrated rate given by the linear curve fit. Table **T9** summarizes estimates of net sulfate reduction rate parameters for Leg 204 sites away from the summit. Figure **F10** shows the rate of sulfate reduction as a function of depth, along with the observed sulfate concentration profile and exponential fit to the data for Site 1244.

T9. Sulfate reduction rate parameters, p. 51.

F10. Sulfate reduction rate, p. 34.

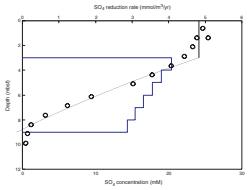

The integrated rates estimated from the exponential gradient are less than those estimated from the linear gradient, but both estimates are subject to uncertainties resulting from the number of factors and assumptions required in the calculations. All of the estimates are the same order of magnitude (14–50 mmol/m^2/yr), with the differences being primarily because of differences in the biostratigraphic sedimentation rates used. The amounts of organic carbon needed to support the calculated rates of sulfate reduction are 0.3–0.5 wt%. Measured organic carbon contents (see individual site chapters in Tréhu, Bohrmann, Rack, Torres, et al., 2003) generally ranged from 0.9 to 1.6 wt%, with no obvious depth-related trends. Average values were 1.1–1.2 wt% at Sites 1245, 1246, 1247, and 1248 and 1.3–1.4 wt% at Sites 1244, 1250, and 1251. Organic carbon contents are mostly residual values measured at depths where intense organic matter remineralization processes are largely completed but in any case are adequate to support the observed extents of sulfate reduction and methanogenesis, as discussed below.

These rates of sulfate reduction can be compared with sulfate reduction rates in other environments. D'Hondt et al. (2004) found a net sulfate reduction rate of 25 mmol/m^2/yr on the slope of the Peru margin, similar to what was observed at nonsummit sites near Hydrate Ridge. In contrast, Boetius et al. (2000) determined gross (radiotracer) volumetric sulfate reduction rates as a function of depth in the upper 15 cm of sediment at the summit of southern Hydrate Ridge. Observed rates beneath sulfide-oxidizing bacterial mats at the ridge crest were 0.5–5 µmol/cm^3/d (1.4–14 mmol/cm^3/yr), and the integrated rate over the 15-cm-thick sulfate reduction zone was 140 mmol/m^2/d, (5.1×10^4 mmol/m^2/yr), or more than 1000 times the calculated net rates of sulfate reduction at sites away from the summit of Hydrate Ridge. This rapid rate of sulfate reduction at the summit is due to the flux of gaseous methane to the seafloor, which supports sulfate reduction coupled with anaerobic methane oxidation (AMO) by the net reaction

$$CH_4 + SO_4^{2-} \rightarrow HCO_3^- + HS^- + H_2O.$$

Some supporting evidence for this process is the occurrence of isotopically light carbonate in the sediments (Greinert et al., 2001), which is a product of oxidized methane.

The pore water chemistry at Leg 204 nonsummit sites can be used to evaluate possible occurrence of methane oxidation. The $\delta^{13}C$ of DIC is shown in Figure **F6.** Only at Sites 1246 and 1245, with minimum $\delta^{13}C$ values of –30‰ and –24‰, respectively, is there possible isotopic evi-

dence for some anaerobic methane oxidation. For example, at Site 1246 the minimum DIC $\delta^{13}C$ value of –30‰ could be produced by mixing ~12.5% DIC of –100‰ from oxidation of the shallowest, earliest-formed microbial methane (70‰ more negative than the DIC from which it is formed) with 87.5% of DIC of –20‰ from the oxidation of sedimentary organic matter.

The DIC $\delta^{13}C$ profiles in Figure F6 are typical of marine sediments in which anaerobic oxidation of organic matter is linked to bacterial sulfate reduction followed by carbonate reduction or methane generation. The DIC produced during sulfate reduction has the same $\delta^{13}C$ as the organic matter undergoing oxidation. Organic carbon in marine sediments of the northeast Pacific generally has $\delta^{13}C$ from –24‰ to –21‰ (Peters et al., 1978; Hedges et al., 1984; Dean et al., 1994). The DIC derived from oxidation of organic matter during sulfate reduction initially mixes with buried seawater DIC of ~0‰ and eventually reaches about the same $\delta^{13}C$ as the oxidized carbon source (Presley and Kaplan, 1968). At the depth where the dissolved sulfate supply is exhausted, the DIC $\delta^{13}C$ has a minimum $\delta^{13}C$ value then reverses and becomes heavier because carbon that is ~70‰ lighter than the DIC pool is being removed to make methane at a faster rate than DIC of –20‰ is being added (Claypool and Kaplan, 1974). If methane were being oxidized at the base of the sulfate reduction zone, the DIC $\delta^{13}C$ values would be much more negative (from –60‰ to –30‰) as observed in sediments at other locations where AMO is apparently taking place (Claypool and Threlkeld, 1983; Claypool et al., 1985, 2003; Vuletich et al., 1989; Blair and Aller, 1995; Burns, 1998; Borowski et al., 2000).

Linear sulfate gradients near the base of the sulfate reduction zone are commonly assumed to result from downward diffusive flux that is balanced by upward diffusive flux of methane, with anaerobic methane oxidation occurring at the base of the sulfate reduction zone (Borowski et al., 1996; Niewöhner et al., 1998; Dickens, 2001). However, equating methane flux with sulfate flux is only valid if there is no sulfate reduction fueled by oxidation of sedimentary organic matter (Haese et al., 2003). Sublinear sulfate gradients do not necessarily require or imply a corresponding equal upward flux of methane and consequent AMO.

In addition to the lack of isotopic evidence for AMO in the DIC $\delta^{13}C$ at most of the Leg 204 nonsummit sites, the pore water chemistry also indicates that oxidation of sedimentary organic matter is the main or exclusive electron donor for sulfate reduction. As indicated earlier, organic matter oxidation produces 2 mol bicarbonate and 0.2 mol ammonia in order to generate the eight electrons required to reduce 1 mol sulfate. Figure F11 shows that bicarbonate production (measured as alkalinity and corrected for cation depletion) is about twice the degree of sulfate depletion within the sulfate reduction zone at Sites 1244, 1245, and 1247. The fact that levels of ammonium and phosphate ions are directly proportional to degree of sulfate depletion also supports sedimentary organic matter oxidation, rather than methane oxidation, as the main source of the electrons used in sulfate reduction at the nonsummit sites.

F11. Sulfate vs. alkalinity, p. 35.

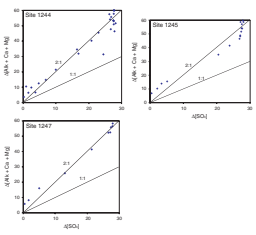

Alkalinity Generation and Microbial Methanogenesis

Oxidation of organic matter in anoxic sediments is a continuous electron- and CO_2-generating process as long as metabolizable organic matter, the required microbial community, and suitable oxidized substances (electron acceptors) are available. When dissolved sulfate is ex-

hausted, dissolved CO_2 becomes the next available electron acceptor (Claypool and Kaplan, 1974). The pH of pore water in marine sediments generally is buffered at 7.7–8.3 by reaction with carbonates and clays. In this pH range, carbonate speciation is such that ~98% of total dissolved CO_2 is present as bicarbonate, and titration alkalinity is a useful proxy for bicarbonate or DIC.

At the depth where sulfate is exhausted, methane concentrations increase and DIC $\delta^{13}C$ shows a marked reversal (Fig. F6) consistent with the onset of methanogenesis and the removal of ^{12}C-enriched CO_2 to produce CH_4. In addition, the alkalinity vs. depth plot generally shows a discontinuity or reversal in concentration at the depth where sulfate is exhausted because of CO_2 removal by microbial methanogenesis. Measured alkalinity at any depth beneath the zone of sulfate reduction is the net of CO_2 addition from organic matter oxidation minus CO_2 removal as methane and authigenic carbonate. Alkalinity production resulting from organic matter oxidation can be projected from the modeled sulfate gradient. The difference between the initial seawater sulfate concentration and the asymptotic sulfate concentration that would have been attained when metabolizable organic matter was exhausted is one-half the projected asymptotic bicarbonate concentration, assuming a 2:1 bicarbonate to sulfate stoichiometry for organic matter oxidation. Therefore, the difference between the projected and observed alkalinity increase during organic matter oxidation is a measure of the amount of CO_2 removed to form methane and authigenic carbonate. A minimum estimate of carbonate precipitation is provided by the cation deficit (Δ[Ca + Mg]) beneath the zone of sulfate reduction, and the amount of methane generated at a given depth can be estimated from the difference between total alkalinity generated minus the sum of remaining alkalinity plus the cation deficit, or

$$CH_4 = Alk_{total} - (Alk_{measured} + \Delta[Ca + Mg]).$$

Total alkalinity generated can be estimated from

$$Alk_{total} = (C_\infty - C_o)(1 - \exp[(-k/\omega)x]) + C_o,$$

where

- C_∞ = asymptotic alkalinity (taken as twice the C_∞ value for sulfate reduction),
- k = rate constant for organic matter oxidation (as determined from the sulfate gradient),
- C_o = initial bicarbonate concentration (2.4 mM),
- ω = burial velocity, and
- x = depth beneath the bioturbation or downwelling zone.

Figure F12 shows concentration trends with depth for dissolved methane and alkalinity at Site 1244. The smooth curve labeled Alk_{total} is an estimate of total alkalinity (bicarbonate) production as a function of depth, calculated from the equation given above. The irregular profile labeled Alk_{obsvd} is the shipboard measured alkalinity, and the irregular profile labeled $CH_{4(calculated)}$ is methane concentration calculated from alkalinity mass balance. The curve labeled $CH_{4(model)}$ is from

$$CH_{4(model)} = f(Alk_{total})(1 - \exp^{[-k/\omega]x}),$$

F12. Alkalinity and methane, p. 36.

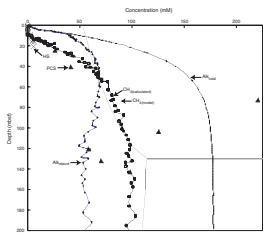

where

f = fraction of total alkalinity converted to methane (0.55–0.60) and
x = depth beneath the sulfate reduction zone.

Also shown on Figure F12 are methane phase relations (solubility curve from spreadsheet of Xu, 2002) and some direct measurements of methane content of Site 1244 sediments, which constrain the estimates of methane concentration presented here. Headspace gas analyses in the shallow sediments indicate that methane is absent within the sulfate reduction zone and begins to build up just beneath it. The six PCS cores show specific intervals of recovered methane content with depth in Site 1244 sediments. The two shallow PCS samples (24 and 40 mbsf) contain methane amounts consistent with only dissolved methane at concentration levels that are undersaturated with respect to methane hydrate (26 and 41 mmol/L of pore volume, respectively). Two intermediate-depth PCS samples (73 and 103 mbsf) have methane contents in excess of methane hydrate saturation (220 and 125 mM, respectively), which presumably consists of dissolved methane at saturation levels and small amounts (10 and 3 vol% of porosity, respectively) of methane hydrate. Three deeper PCS samples near the base of gas hydrate stability (120, 131 and 142 mbsf) are again undersaturated relative to methane hydrate and/or free gas. These PCS measurements are all consistent with the estimated quantities of methane generated as a function of depth in that PCS measurements indicate methane contents above saturation in the depth interval (44–113 mbsf) where the calculated methane contents exceed the theoretical solubility curve, and methane contents below saturation above and beneath this depth interval.

An additional constraint is provided by the observation that the shallowest chlorinity anomaly and occurrence of methane hydrate at Site 1244 was at ~45 mbsf (Milkov et al., 2004a; Tréhu et al., 2004). The calculated and modeled dissolved methane contents at Site 1244 also just exceeded saturation levels (~66 mM) at that same depth.

Similar results were obtained by modeling alkalinity and methane generation at the other nonsummit sites (1245, 1246, 1247, 1251, and 1252). The volumetric (mmol/m³/yr) rates of methane generation for Site 1244 are shown in Figure F13. These rates were integrated over interval 8–150 mbsf to give net integrated rates of methane production (mmol/m²/yr) for Leg 204 sites shown in Table T10.

F13. Methane production rate, p. 37.

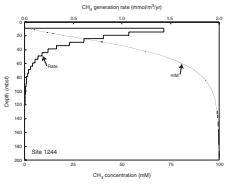

T10. Methane production rate parameters, p. 52.

Ethane Generation Mechanisms

Core void gas samples in marine sediments at shallow depths of burial are usually composed of methane (99.99+% on an air-free basis) with traces of ethane, propane, and carbon dioxide and variable air contamination. Ethane (C_2H_6) is the most abundant and frequently the only higher carbon–number (C_{2+}) hydrocarbon detected in shipboard analyses of gases from cores. At least three mechanisms can account for ethane content of gases: microbial processes, low-temperature (<80°C) decomposition of organic matter, and migration of higher-temperature (>80°C) gas of thermogenic origin from deeper sediments. Evidence that microbial processes account for some ethane is the extremely light ^{13}C-depleted ethane found in some gases of microbial origin (Mattavelli et al., 1992; Waseda and Didyk, 1995; Paull et al., 2000; Taylor et al., 2000). Microbial ethane could arise during methanogenesis if two-car-

bon organic acids (acetate and oxalate) can also be used, like CO_2 as electron acceptors (Claypool, 1999). Evidence for microbial ethane from organic acid reduction is present in the form of isotopically heavy calcium oxalate minerals (Hoefs, 1969; Zak and Skala, 1993) and in organic acids in formation waters with carboxyl carbon having $\delta^{13}C$ as heavy as +38‰ (Franks et al., 1997). These could represent residual carbon pools that have undergone some conversion to ethane with a large kinetic isotopic fractionation. Alternatively, there is some evidence for enzyme-catalyzed carbon isotopic exchange between dissolved CO_2 and carboxyl carbon of organic acids (O'Leary and Yapp, 1978). Such exchange would imply organic acids coexisting with dissolved CO_2 depleted in ^{13}C by methanogenesis, but not necessarily acting as alkane precursors.

Migrated ethane (usually accompanied by other C_{2+} alkanes) of obvious deep thermogenic origin is occasionally encountered at shallow depths in marine sediments at Hydrate Ridge and elsewhere (Schumacher and Abrams, 1996) and requires existence of some migration conduit.

The most common mechanism for ethane generation in marine sediments at relatively shallow (<1 km) depths of burial is low-temperature decomposition of sedimentary organic matter. DSDP/ODP cored sediments almost invariably show an exponential increase in ethane (as shown by C_1/C_2) with increasing temperature and depth of burial. The increase in C_1/C_2 ratio in core gas void samples from sediments that contain microbial methane is directly related to temperature history of the sediment. A simple kinetic calculation can reproduce most observed trends of C_1/C_2 in a range of sedimentary environments with widely varying temperature histories (Claypool, 1974). The inputs for such a calculation are sedimentation rate and geothermal gradient (heating rate) and kinetic constants for low-temperature ethane generation ($A = 10^{14}$/s, E = 10 kJ/mol). Examples of observed C_1/C_2 ratios in sediments with differing thermal histories are illustrated in Figure **F14.** The appearance of increasing amounts of ethane and propane is frequently interpreted as a flux of thermogenic gas from deeply buried sediments; however, this interpretation is only warranted if quantities of ethane exceed that expected from the low-temperature decomposition of the buried organic matter.

F14. DSDP/ODP C_1/C_2 ratios, p. 38.

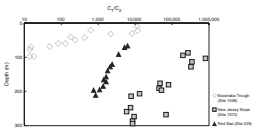

Possible groupings of ethane of different origins according to $\delta^{13}C$ and C_1/C_2 are shown in Figure **F4.** Samples that contain large amounts of microbial ethane have $\delta^{13}C$ values from –55‰ to –45‰ and C_1/C_2 ratios >20,000. Microbial ethane is mostly in samples of hydrate-bound gases with no influence of migrated thermogenic ethane. The samples representing proposed low-temperature thermogenic or diagenetic ethane are mainly void gas samples from the slope basin sites (1244, 1251, and 1252). Samples dominated by migrated thermogenic ethane were from core gas voids at depths in and near Horizon A at Sites 1245, 1247, and 1248. The samples that plot between the diagenetic and thermogenic ethane fields are mostly near-surface hydrate-bound gas from the summit sites (1249 and 1250) and probably represent thermogenic ethane overprinted or mixed with some diagenetic or microbial ethane.

Ethane Fractionation by Gas Hydrate Formation

High-resolution gas geochemistry during Leg 204 showed that gases within the GHSZ at some nonsummit sites do not have the expected increase in ethane (i.e., are depleted in ethane), whereas those just below

the GHSZ show a sharp (~10×) increase in ethane content (Tréhu, Bohrmann, Rack, Torres, et al., 2003; Milkov et al., 2004a). The ethane depletion of void gas samples within the GHSZ is associated with gas hydrate occurrence and is due to formation of Structure I gas hydrates, which are enriched in ethane relative to the dissolved gas from which they are formed (Sloan, 1998). Gas samples from core voids formed within the GHSZ were mainly from residual dissolved methane that is depleted in ethane resulting from gas hydrate formation, although some core voids at the top of the gas hydrate occurrence zone were from decomposed gas hydrate and showed some relative C_2 enrichment (Milkov et al., 2004a). This molecular fractionation characteristic of gas hydrate occurrence is most apparent in the shallow microbial gas in slope basin sediments adjacent to Hydrate Ridge, where there is no influx of gas from the deeper subsurface (Milkov et al., 2005).

Such departure from the normal trend of absolute and relative ethane content is illustrated in Figure **F15B** and **F15C** for analyses of void gas samples from Sites 1244 and 1251. Here there are major discontinuities in ethane content occurring at depths corresponding to the pressure-temperature base of gas hydrate stability at each site.

Ethane enrichment in void gas samples below the base of gas hydrate stability was also observed during Leg 204 at Sites 1245, 1247, 1248, and 1250 (Tréhu, Bohrmann, Rack, Torres, et al., 2003). However, ethane distribution at these other Leg 204 sites is complicated by the presence of migrated thermogenic hydrocarbons (Milkov et al., 2005).

Comparison of C_1/C_2 in void gases and in hydrate-bound gases indicates that gas hydrate shows the expected C_2 enrichment. Moreover, hydrate-bound gases do not contain C_3, which is excluded by Structure I gas hydrate (Sloan, 1998). Calculations using the CSMHYD program (Sloan, 1998) show that the mole fraction of C_2 in gas hydrate has a four-fold enrichment over the mole fraction of C_2 in the gas from which the gas hydrate was formed.

The solid line in the C_1/C_2 plots of Figure **F15A, F15B,** and **F15C** shows the expected C_1/C_2 trends based on heating rate at Sites 1244, 1251, and 1252. The void gas samples from Site 1252 generally follow the expected trend with no obvious C_2 depletions or enrichments above or below the base of gas hydrate stability. At Site 1252, there is no BSR, no chlorinity anomalies, and apparently little or no significant development of gas hydrates, although adequate CH_4 contents were estimated by the model discussed above. In contrast at Sites 1244 and 1251 and compared with the expected trend of C_1/C_2, there is apparent C_2 depletion above and enrichment below the base of gas hydrate stability, producing a significant offset in C_1/C_2 ratio at the respective depths (125 and 195 mbsf) of the base of gas hydrate stability. Void gas samples within the GHSZ are depleted in C_2 because it has been selectively removed from the dissolved gas in the pore water and is being stored as gas hydrate in the solid phase of the sediment. As the sediment layers subside beneath the P-T horizon, marking the base of gas hydrate stability, the gas hydrate decomposes and releases C_2-enriched gas, causing the observed relative C_2 enrichment in the dissolved (or free) gas below the GHSZ at Sites 1251 and 1244.

The chemical fractionation at the base of gas hydrate stability is enhanced by the fact that a C_2-enriched solid (gas hydrate) subsides more rapidly than pore water with dissolved gas because of compaction. This differential subsidence effectively transfers ethane from the dissolved

F15. C_1/C_2 ratios vs. depth, p. 39.

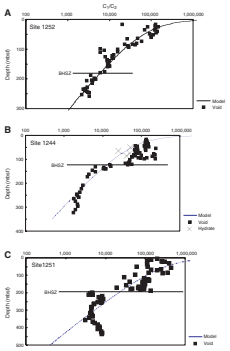

phase above the base of gas hydrate stability to the dissolved (and gas) phase beneath the base of gas hydrate stability.

The discontinuity in C_1/C_2 at the base of gas hydrate stability could be developed as a quantitative indicator of gas hydrate abundance and is present in some previously cored ODP holes, such as at ODP Site 1019 in the Eel River Basin (Fig. F16). However, the C_1/C_2 discontinuity has not been observed at some other sites where gas hydrates were present, in part because of insufficient sample frequency, but probably also because of differences in the mode of gas hydrate formation.

F16. Eel River Basin C_1/C_2 ratios, p. 40.

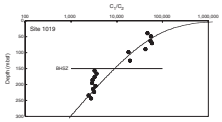

SUMMARY AND CONCLUSIONS

Geochemical analyses carried out on samples collected from cores on and near the southern summit of Hydrate Ridge have advanced understanding by providing a clear contrast of the two major modes of marine gas hydrate occurrence. High concentrations (15%–40% of pore space) of gas hydrate occurring at shallow depths (0–40 mbsf) on and near the southern summit are fed by gas migrating from depths of as much as 2 km within the accretionary prism. This gas carries a characteristic minor component of C_2–C_5 thermogenic hydrocarbons that enable tracing of migration pathways and may stabilize the occurrence of some Structure II gas hydrate. A Structure II wet gas hydrate that is stable to greater depths and temperatures than Structure I methane hydrate may account for the deeper, faint second bottom simulating reflection (BSR_2) that occurs on the seaward side of the ridge. The wet gas is migrating in an ash/turbidite layer that intersects the base of gas hydrate stability on the seaward side of and directly beneath the southern summit of Hydrate Ridge. The high gas saturation (>65%) of the pore space within this layer could create a two-phase (gas + solid) system that would enable free gas to move vertically upward through the gas hydrate stability zone.

Away from the summit of the ridge there is no apparent influx of the gas seeping from depth and sediments are characterized by the normal sequence of early diagenetic processes involving anaerobic oxidation of sedimentary organic matter, initially linked to the reduction of sulfate and later continued by means of carbonate reduction leading to the formation of microbial methane. A well-defined sulfate/methane interface occurs at each of the sites cored away from the summit, but there is apparently little or no anaerobic methane oxidation occurring, as evidenced by the fact that all except one site lack any dissolved inorganic carbon more ^{12}C enriched than about –24‰ at the sulfate/methane interface. The observed concentration gradients in sulfate, alkalinity, and methane are more a product of rapid reactions than diffusive fluxes. The concentration gradients and sedimentation rates provide estimates of the rates of microbial sulfate reduction and methane generation. Observed rates at sites away from the summit are comparable to those found in other high-productivity continental margin settings but are three orders of magnitude slower than rates of microbial processes occurring at the summit of southern Hydrate Ridge.

The microbial methane within a 100-m thickness of these sediments is generated over a period of some 200,000–300,000 yr, and the pressure conditions at Hydrate Ridge have changed dramatically during the last 100,000 yr as a result of tectonic uplift. It is probably the lowering of methane solubility requirements associated with this pressure reduction (from 30 to 8 MPa) more than particularly vigorous methane gen-

eration that brings about gas venting and widespread gas hydrate occurrence on the Cascadia and other active margins.

ACKNOWLEDGMENTS

This research used samples and/or data provided by the Ocean Drilling Program (ODP). ODP was sponsored by the U.S. National Science Foundation (NSF) and participating countries under management of Joint Oceanographic Institutions (JOI), Inc. Funding for this research was provided by the U.S. Science Support Program. We acknowledge the help of the Leg 204 Science Party and the ODP technical staff in carrying out the Leg 204 geochemistry program. We thank Amane Waseda and an anonymous reviewer for constructive suggestions.

REFERENCES

Berner, R.A., 1980. *Early Diagenesis: A Theoretical Approach:* Princeton, NJ (Princeton Univ. Press).

Blair, N.E., and Aller, R.C., 1995. Anaerobic methane oxidation on the Amazon Shelf. *Geochim. Cosmochim. Acta,* 59:3707–3715. **doi:10.1016/0016-7037(95)00277-7**

Boetius, A., Ravenschlag, K., Schubert, C.J., Rickert, D., Widdel, F., Gieseke, A., Amann, R., Jørgensen, B.B., Witte, U., and Pfannkuche, O., 2000. A marine microbial consortium apparently mediating anaerobic oxidation of methane. *Nature (London, U. K.),* 407:623–626. **doi:10.1038/35036572**

Boetius, A., and Suess, E., 2004. Hydrate Ridge: a natural laboratory for the study of microbial life fueled by methane from near surface gas hydrates. *Chem. Geol.,* 205:291–310. **doi:10.1016/j.chemgeo.2003.12.034**

Borowski, W.S., Hoehler, T.M., Alperin, M.J., Rodriguez, N.M., and Paull, C.K., 2000. Significance of anaerobic methane oxidation in methane-rich sediments overlying the Blake Ridge gas hydrates. *In* Paull, C.K., Matsumoto, R., Wallace, P.J., and Dillon, W.P. (Eds.), *Proc. ODP, Sci. Results,* 164: College Station, TX (Ocean Drilling Program), 87–99. [**HTML**]

Borowski, W.S., Paull, C.K., and Ussler, III, W., 1996. Marine pore-water sulfate profiles indicate in situ methane flux from underlying gas hydrate. *Geology,* 24(7):655–658. **doi:10.1130/0091-7613(1996)024<0655:MPWSPI>2.3.CO;2**

Burns, S.J., 1998. Carbon isotopic evidence for coupled sulfate reduction-methane oxidation in Amazon Fan sediments. *Geochim. Cosmochim. Acta,* 62:797–804. **doi:10.1016/S0016-7037(98)00035-0**

Canfield, D.E., 1991. Sulfate reduction in deep-sea sediments. *Am. J. Sci.,* 291:177–188.

Chung, H.M., Gromly, J.R., and Squires, R.M., 1988. Origin of gaseous hydrocarbons in subsurface environments: theoretical considerations of carbon isotope distribution. *Chem. Geol.,* 71:97–104. **doi:10.1016/0009-2541(88)90108-8**

Claypool, G.E., 1974. Anoxic diagenesis and bacterial methane production in deep sea sediments [Ph.D. thesis]. Univ. California, Los Angeles.

Claypool, G.E., 1999. Biogenic ethane—where does it come from? *In* Schoell, M., and Claypool, G.E. (Eds.), *Abstract volume, AAPG Hedberg Res. Conf.: Natural Gas Formation and Occurrence.*

Claypool, G.E., and Kaplan, I.R., 1974. The origin and distribution of methane in marine sediments. *In* Kaplan, I.R. (Ed.), *Natural Gases in Marine Sediments:* New York (Plenum), 99–139.

Claypool, G.E., Lorenson, T.D., and Johnson, C.A., 2003. Authigenic carbonates, methane generation, and oxidation in continental rise and shelf sediments, ODP Leg 188 Sites 1165 and 1166, offshore Antarctica (Prydz Bay). *In* Cooper, A.K., O'Brien, P.E., and Richter, C. (Eds.), *Proc. ODP, Sci. Results,* 188, 1–15 [Online]. Available from World Wide Web: <**http://www-odp.tamu.edu/publications/188_SR/VOLUME/CHAPTERS/004.PDF**>. [Cited 2005-01-20]

Claypool, G.E., and Threlkeld, C.N., 1983. Anoxic diagenesis and methane generation in sediments of the Blake Outer Ridge, Deep Sea Drilling Project Site 533, Leg 76. *In* Sheridan, R.E., Gradstein, F.M., et al., *Init. Repts. DSDP,* 76: Washington (U.S. Govt. Printing Office), 391–402.

Claypool, G.E., Vuletich, A.K., and Kvenvolden, K.A., 1985. Isotopic composition of interstitial fluids in sediment of the Nankai Trough, Deep Sea Drilling Project Leg 87. *In* Kagami, H., Karig, D.E., Coulbourn, W.T., et al., *Init. Repts. DSDP,* 87: Washington (U.S. Govt. Printing Office), 857–860.

Dean, W.E., Gardner, J.V., and Anderson, R.Y., 1994. Geochemical evidence for enhanced preservation of organic matter in the oxygen minimum zone of the continental margin of northern California during the late Pleistocene. *Paleoceanography,* 9:47–62. **doi:10.1029/93PA02829**

de Boer, R.B., Houbolt, J.J.H.C., and Legrand, J., 1985. Formation of gas hydrates in a permeable medium. *Geol. Mijnbouw,* 64:245–249.

D'Hondt, S.L., Jørgensen, B.B., Miller, D.J., Batzke, A., Blake, R., Cragg, B.A., Cypionka, H., Dickens, G.R., Ferdelman, T., Hinrichs, K.-H., Holm, N.G., Mitterer, R., Spivack, A., Wang, G., Bekins, B., Engelen, B., Ford, K., Gettemy, G., Rutherford, S.D., Sass, H., Skilbeck, C.G., Aiello, I.W., Guerin, G., House, C., Inagak, F., Meister, P., Naehr, T., Niitsuma, S., Parkes, R.J., Schippers, A., Smith, D.C., Teske, A., Wiegel, J., Naranjo Padillo, C., and Solis Acosta, J.L., 2004. Distributions of microbial activities in deep subseafloor sediments. *Science,* 306:2216–2221. **doi:10.1126/science.1101155**

Dickens, G.R., 2001. Sulfate profiles and barium fronts in sediment on the Blake Ridge: present and past methane fluxes through a large gas hydrate reservoir. *Geochim. Cosmochim. Acta,* 65:529–543. **doi:10.1016/S0016-7037(00)00556-1**

Flemings, P.B., Liu, X., and Winters, W.J., 2003. Critical pressure and multiphase flow in Blake Ridge gas hydrates. *Geology,* 31:1057–1060. **doi:10.1130/G19863.1**

Franks, S.G., Boles, J.R., Fincannon, A.L., Freeman, K.H., Holba, A.G., and Jordan, E.D., 1997. Carbon isotopic composition of organic acids in oilfield waters, San Joaquin basin, California. *AAPG 1997 Annu. Conv.,* 6:37. (Abstract)

Grauls, D., 2001. Gas hydrates: importance and applications in petroleum exploration. *Mar. Pet. Geol.,* 18:519–523. **doi:10.1016/S0264-8172(00)00075-1**

Greinert, J., Bohrmann, G., and Suess, E., 2001. Gas hydrate-associated carbonates and methane venting at Hydrate Ridge: classification, distribution, and origin of authigenic lithologies. *In* Paull, C.K., Dillon, W.P. (Eds.), *Natural Gas Hydrates: Occurrence, Distribution, and Dynamics*. Gephys. Monogr., 124:99–113.

Haese, R.R., Meile, C., Van Cappellen, P., and De Lange, G., 2003. Carbon geochemistry of cold seeps: methane fluxes and transformation in sediments from Kazan mud volcano, eastern Mediterranean Sea. *Earth Planet. Sci. Lett.,* 212:361–375. **doi:10.1016/S0012-821X(03)00226-7**

Hedges, J.I., Turin, H.J., and Ertel, J.R., 1984. Sources and distributions of sedimentary organic matter in the Columbia River drainage basin, Washington and Oregon. *Limnol. Oceanogr.,* 29:35–46.

Heeschen, K.U., Tréhu, A.M., Collier, R.W., Suess, E., and Rehder, G., 2003. Distribution and height of methane bubble plumes on the Cascadia margin characterized by acoustic imaging. *Geophys. Res. Lett.,* 30:1643–1646. **doi:10.1029/2003GL016974**

Hoefs, J., 1969. Natural calcium oxalate with heavy carbon. *Nature (London, U. K.),* 223:396.

Hornbach, M.J., Saffer, D.M., and Holbrook, W.S., 2004. Critically pressured free-gas reservoirs below gas-hydrate provinces. *Nature (London, U. K.),* 427:142–144. **doi:10.1038/nature02172**

Hovland, M., Lysne, D., and Whiticar, M., 1995. Gas hydrate and sediment gas composition, Hole 892A. *In* Carson, B., Westbrook, G.K., Musgrave, R.J., and Suess, E. (Eds.), *Proc. ODP, Sci. Results,* 146 (Pt 1): College Station, TX (Ocean Drilling Program), 151–161.

Hyndman, R.D., and Spence, G.D., 1992. A seismic study of methane hydrate marine bottom simulating reflectors. *J. Geophys. Res.,* 97:6683–6698.

Jørgensen, B.B., Böttcher, M.E., Lüschen, H., Neretin, L.N., and Volkov, I.I., 2004. Anaerobic methane oxidation and a deep H_2S sink generate isotopically heavy sulfides in Black Sea sediments. *Geochim. Cosmochim. Acta,* 68:2095–2118. **doi:10.1016/j.gca.2003.07.017**

Kastner, M., Kvenvolden, K.A., and Lorenson, T.D., 1998. Chemistry, isotopic composition, and origin of a methane-hydrogen sulfide hydrate at the Cascadia subduction zone. *Earth Planet. Sci. Lett.,* 156:173–183. **doi:10.1016/S0012-821X(98)00013-2**

Mattavelli, L., Ricchiuto, T., and Martinenghi, C., 1992. Deep isotopic light methane in northern Italy. *In* Vially, R. (Ed.), *Bacterial Gas:* Paris (Technip), 121–132.

McKay, M.E., Moore, G.F., Cochrane, G.R., Moore, J.C., and Kulm, L.D., 1992. Landward vergence and oblique structural trends in the Oregon margin accretionary prism: implications and effect on fluid flow. *Earth Planet. Sci. Lett.,* 109:477–491. **doi:10.1016/0012-821X(92)90108-8**

Milkov, A.V., Claypool, G.E., Lee, Y.-J., and Sassen, R., 2005. Gas hydrate systems at Hydrate Ridge offshore Oregon inferred from molecular and isotopic properties of gas hydrate-bound and void gases. *Geochim. Cosmochim. Acta,* 69(4):1007–1026. **doi:10.1016/j.gca.2004.08.021**

Milkov, A.V., Claypool, G.E., Lee, Y.-J., Torres, M.E., Borowski, W.S., Tomaru, H., Sassen, R., Long, P.E., and the ODP Leg 204 Scientific Party, 2004a. Ethane enrichment and propane depletion in subsurface gases indicate gas hydrate occurrence in marine sediments at southern Hydrate Ridge offshore Oregon. *Org. Geochem.,* 35:1067–1080. **doi:10.1016/j.orggeochem.2004.04.003**

Milkov, A.V., Claypool, G.E., Lee, Y-J., Xu, W., Dickens, G.R., Borowski, W.S., and the ODP Leg 204 Scientific Party, 2003. In situ methane concentrations at Hydrate Ridge offshore Oregon: new constraints on the global gas hydrate inventory from an active margin. *Geology,* 31:833–836.

Milkov, A.V., Dickens, G.R., Claypool, G.E., Lee, Y-J., Borowski, W.S., Torres, M.E., Xu, W., Tomaru, H., Tréhu, A.M., and Schultheiss, P., 2004b. Co-existence of gas hydrate, free gas, and brine within the regional gas hydrate stability zone at Hydrate Ridge (Oregon margin): evidence from prolonged degassing of a pressurized core. *Earth Planet. Sci. Lett.,*222:829–843. **doi:10.1016/j.epsl.2004.03.028**

Niewöhner, C., Henson, C., Kasten, S., Zabel, M., and Schultz, H.D., 1998. Deep sulfate reduction completely mediated by anaerobic methane oxidation in sediments of the upwelling area off Nambia. *Geochim. Cosmochim. Acta,* 62:455–464. **doi:10.1016/S0016-7037(98)00055-6**

O'Leary, M.H., and Yapp, C.J., 1978. Equilibrium carbon isotope effect on a decarboxylation reaction. *Biochem. Biophys. Res. Commun.,* 80:155–160.

Paull, C.K., Lorensen, T.D., Borowski, W.S., Ussler, W., III, Olsen, K., and Rodriguez, N.M., 2000. Isotopic composition of CH_4, CO_2 species, and sedimentary organic matter within samples from the Blake Ridge: gas source implications. *In* Paull, C.K., Matsumoto, R., Wallace, P.J., and Dillon, W.P. (Eds.), *Proc. ODP, Sci. Results,* 164: College Station, TX (Ocean Drilling Program), 67–78. [**HTML**]

Peters, K.E., Sweeney, R.E., and Kaplan, I.R., 1978. Correlation of carbon and nitrogen stable isotope ratios in sedimentary organic matter. *Limnol. Oceanogr.,* 23:598–604.

Pimmel, A., and Claypool, G., 2001. Introduction to shipboard organic geochemistry on the *JOIDES Resolution. ODP Tech. Note,* 30 [Online]. Available from World Wide Web: <**http://www-odp.tamu.edu/publications/tnotes/tn30/INDEX.HTM**>. [Cited 2003-10-10]

Presley, B.J., and Kaplan, I.R., 1968. Changes in dissolved sulfate, calcium and carbonate from interstitial water of near shore sediments. *Geochim. Cosmochim. Acta,* 32:1037–1049. **doi:10.1016/0016-7037(68)90106-3**

Rooney, M.A., Claypool, G.E., and Chung, H.M., 1995. Modeling thermogenic gas generation using carbon isotope ratios of natural gas hydrocarbons. *Chem. Geol.,*126:219–232. **doi:10.1016/0009-2541(95)00119-0**

Schumacher, D., and Abrams, M.A., 1996. Hydrocarbon migration and its near-surface expression. *AAPG Mem.,* 66:446.

Shipboard Scientific Party, 2003a. Explanatory notes. *In* Tréhu, A.M, Bohrmann, G., Rack, F.R., Torres, M.E., et al., *Proc. ODP, Init. Repts.,* 204, 1–102 [CD-ROM]. Available from: Ocean Drilling Program, Texas A&M University, College Station TX 77845-9547, USA. [**HTML**]

Shipboard Scientific Party, 2003b. Site 1245. *In* Tréhu, A.M, Bohrmann, G., Rack, F.R., Torres, M.E., et al., *Proc. ODP, Init. Repts.,* 204, 1–131 [CD-ROM]. Available from: Ocean Drilling Program, Texas A&M University, College Station TX 77845-9547, USA. [**HTML**]

Shipboard Scientific Party, 2003c. Site 1247. *In* Tréhu, A.M, Bohrmann, G., Rack, F.R., Torres, M.E., et al., *Proc. ODP, Init. Repts.,* 204, 1–84 [CD-ROM]. Available from: Ocean Drilling Program, Texas A&M University, College Station TX 77845-9547, USA. [**HTML**]

Shipboard Scientific Party, 2003d. Site 1248. *In* Tréhu, A.M, Bohrmann, G., Rack, F.R., Torres, M.E., et al., *Proc. ODP, Init. Repts.,* 204, 1–75 [CD-ROM]. Available from: Ocean Drilling Program, Texas A&M University, College Station TX 77845-9547, USA. [**HTML**]

Sloan, E.D., 1998. *Clathrate Hydrates of Natural Gases* (2nd ed.): New York (Marcel Dekker).

Suess, E., Torres, M.E., Bohrmann, G., Collier, R.W., Greinert, J., Linke, P., Rehder, G., Tréhu, A., Wallmann, K., Winckler, G., and Zuleger, E., 1999. Gas hydrate destabilization: enhanced dewatering, benthic material turnover and large methane plumes at the Cascadia convergent margin. *Earth Planet. Sci. Lett.,*170:1–15. **doi:10.1016/S0012-821X(99)00092-8**

Taylor, S.W., Sherwood Lollar, B., and Wassenaar, L.I., 2000. Bacteriogenic ethane in near-surface aquifers: implications for leaking hydrocarbon well bores. *Environ. Sci. Technol.,* 34:4727–4732. **doi:10.1021/es001066x**

Torres, M.E., McManus, J., Hammond, D.E., de Angelis, M.A., Heeschen, K.U., Colbert, S.L., Tryon, M.D., Brown, K.M., and Suess, E., 2002. Fluid and chemical fluxes in and out of sediments hosting methane hydrate deposits on Hydrate Ridge, OR, I: Hydrological provinces. *Earth Planet. Sci. Lett.,* 201:525–540. **doi:10.1016/S0012-821X(02)00733-1**

Torres, M.E., Wallmann, K., Tréhu, A.M., Bohrmann, G., Borowski, W.S., and Tomaru, H., 2004. Gas hydrate growth, methane transport, and chloride enrichment at the southern summit of Hydrate Ridge, Cascadia margin off Oregon. *Earth Planet. Sci. Lett.,* 226:225–241. **doi:10.1016/j.epsl.2004.07.029**

Tréhu, A.M, Bohrmann, G., Rack, F.R., Torres, M.E., et al., 2003. *Proc. ODP, Init. Repts.,* 204 [Online]. Available from World Wide Web: <**http://www-odp.tamu.edu/publications/204_IR/204ir.htm**>. [Cited 2003-11-24]

Tréhu, A.M., Long, P.E., Torres, M.E., Bohrmann, G., Rack, F.R., Collett, T.S., Goldberg, D.S., Milkov, A.V., Riedel, M., Schultheiss, P., Bangs, N.L., Barr, S.R., Borowski, W.S., Claypool, G.E., Delwiche, M.E., Dickens, G.R., Gracia, E., Guerin, G., Holland, M., Johnson, J.E., Lee, Y.-J., Liu, C.-S., Su, X., Teichert, B., Tomaru, H., Vanneste, M., Watanabe, M., and Weinberger, J.L., 2004. Three-dimensional distribution of gas hydrate beneath southern Hydrate Ridge: constraints from ODP Leg 204. *Earth Planet. Sci. Lett.,* 222:845–862. **doi:10.1016/j.epsl.2004.03.035**

Tréhu, A.M., Torres, M.E., Moore, G.F., Suess, E., and Bohrmann, G., 1999. Temporal and spatial evolution of a gas-hydrate-bearing accretionary ridge on the Oregon continental margin. *Geology,* 27(10):939–942. **doi:10.1130/0091-7613(1999)027<0939:TASEOA>2.3.CO;2**

Vuletich, A.K., Threlkeld, C.N., and Claypool, G.E., 1989. Isotopic composition of gases and interstitial fluids in sediment of the Vøring Plateau, ODP Leg 104, Site 644. *In* Eldholm, O., Thiede, J., Taylor, E., et al., *Proc. ODP, Sci. Results,* 104: College Station, TX (Ocean Drilling Program), 281–283.

Waseda, A., and Didyk, B.M., 1995. Isotope compositions of gases in sediments from the Chile continental margin. *In* Lewis, S.D., Behrmann, J.H., Musgrave, R.J., and Candy, S.C., (Eds.), *Proc. ODP, Sci. Results,* 141: College Station, TX (Ocean Drilling Program), 307–312.

Xu, W., 2002. Phase balance and dynamic equilibrium during formation and dissociation of methane gas hydrate. *Fourth Int. Conf. Gas Hydrates,* 19023:199–200.

Zak, K., and Skala, R., 1993. Carbon isotopic composition of whewellite ($CaC_2O_4 \cdot H_2O$) from different geological environments and its significance. *Chem. Geol.,* 106:123–131. **doi:10.1016/0009-2541(93)90169-J**

Figure F1. Location of Leg 204 Sites and bathymetry in the vicinity of the southern summit of Hydrate Ridge (Tréhu, Bohrmann, Rack, Torres, et al., 2003).

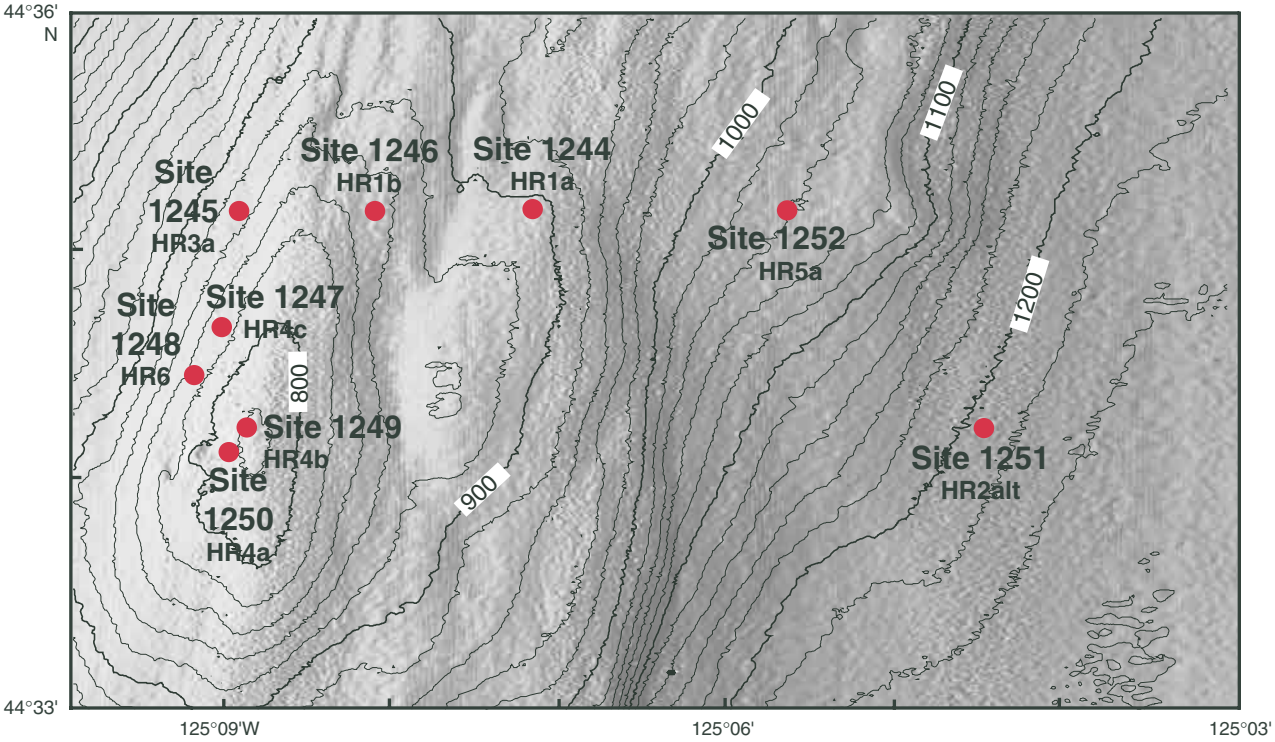

Figure F2. Plots of C_1/C_2 ratios of void gas samples as a function of depth of burial. **A.** Gas samples from Sites 1245 and 1247 on seaward side of Hydrate Ridge that penetrate Horizon A. **B.** Gas samples from Sites 1244, 1246, 1251, and 1252 on landward side of Hydrate Ridge. **C.** Gas samples from Sites 1248, 1249, and 1250 at or near the southern summit of Hydrate Ridge.

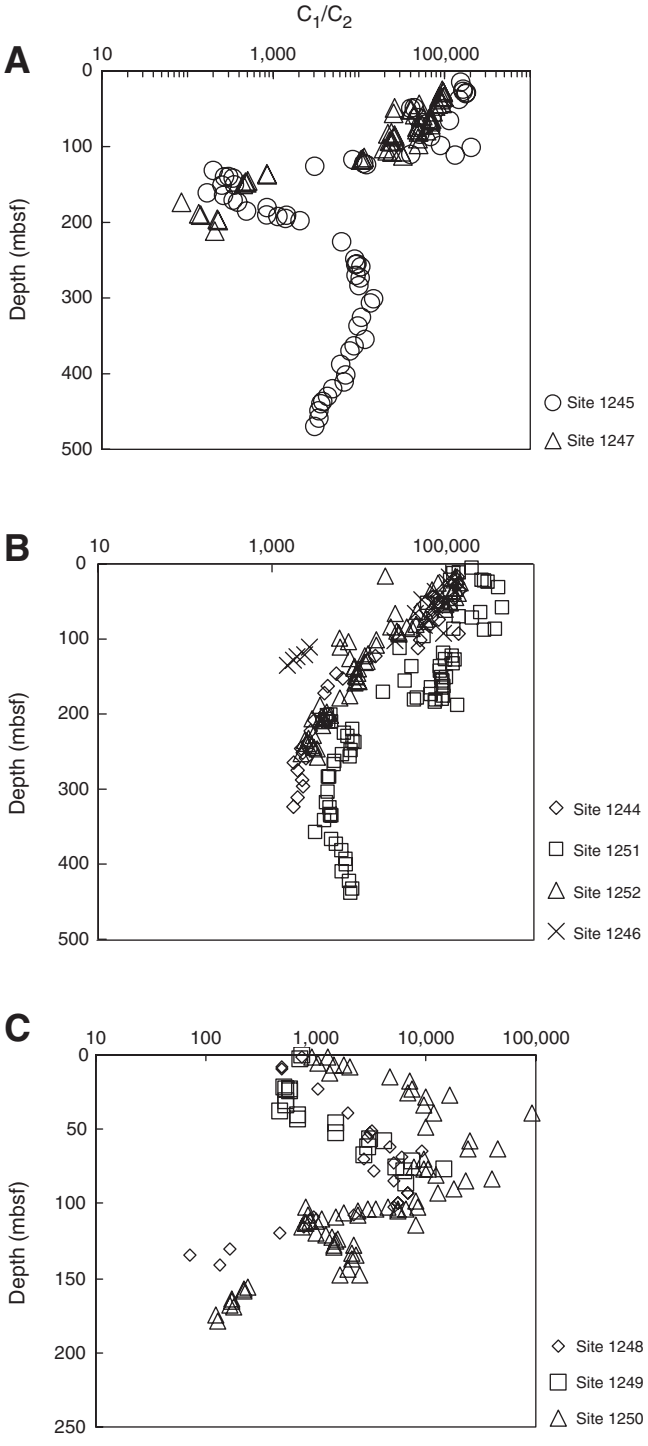

Figure F3. Plot of methane $\delta^{13}C$ of void gas samples as a function of burial depth. **A.** Gas samples from Sites 1244, 1246, 1251, and 1252 on landward side of Hydrate Ridge. **B.** Gas samples from Sites 1245 and 1247 on seaward side of Hydrate Ridge that penetrate Horizon A. **C.** Gas samples from Sites 1248, 1249, and 1250 at or near the southern summit of Hydrate Ridge.

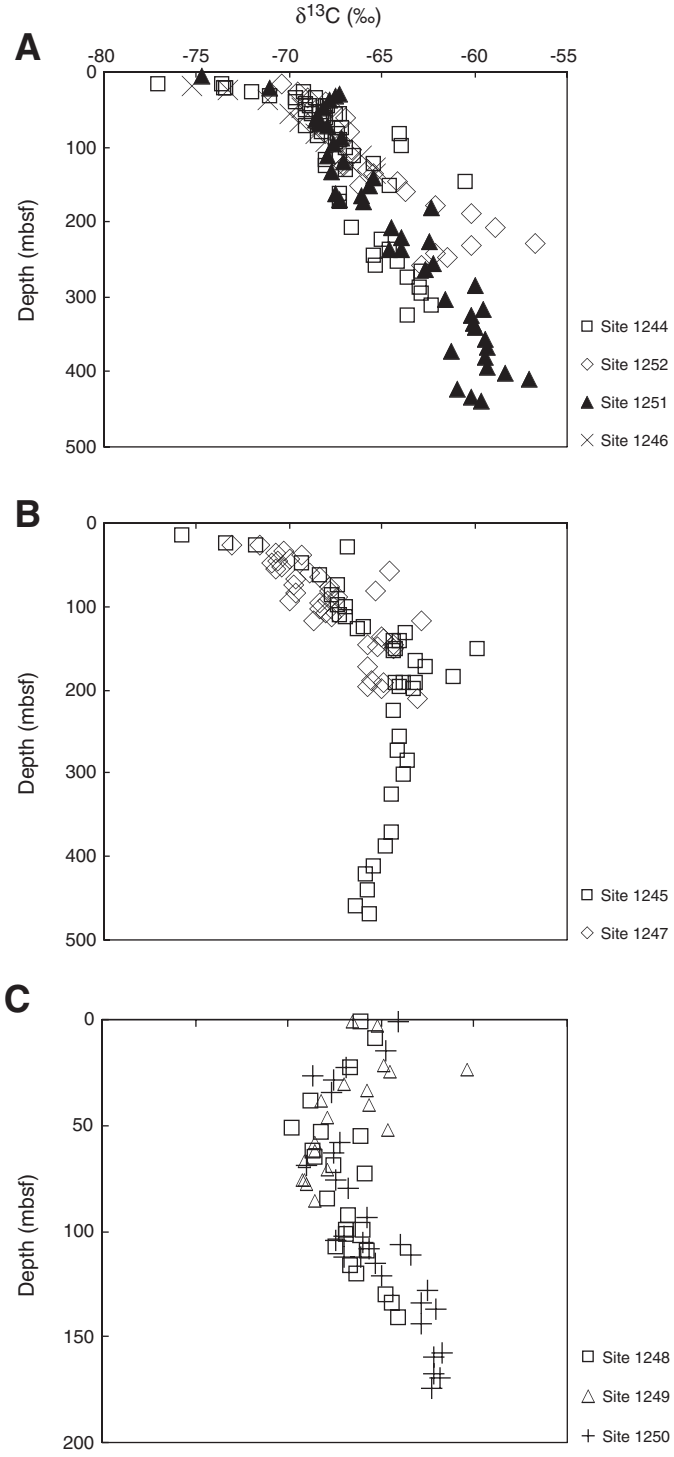

Figure F4. Carbon isotopic composition of ethane component of gas samples plotted against the C_1/C_2 ratio of the gas. Samples are coded by the last two digits of the site numbers, with open symbols and crosses representing hydrate-bound gases.

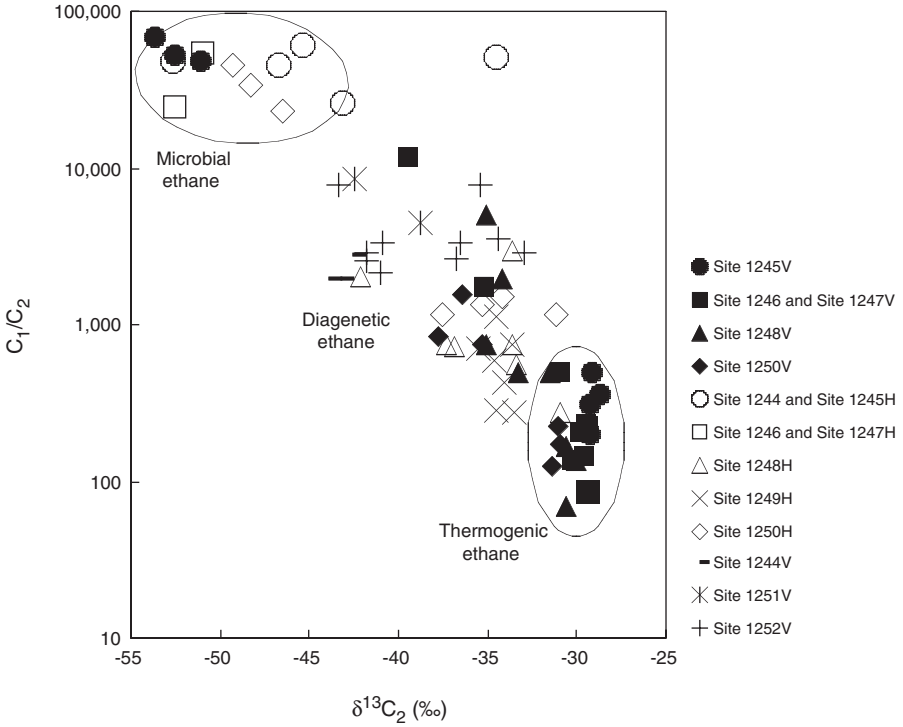

Figure F5. Carbon isotopic composition of methane from pressure core sampler outgassing experiments. PCS gases generally have the same composition as nearby void gas samples.

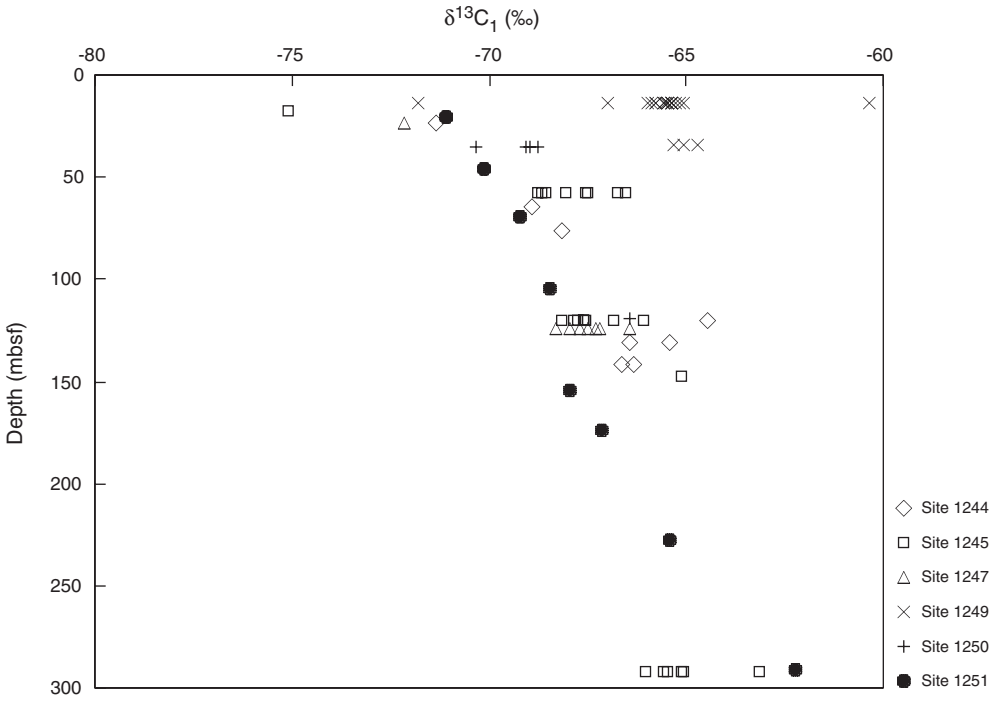

Figure F6. Carbon isotopic composition of dissolved inorganic carbon of interstitial waters from nonsummit sites.

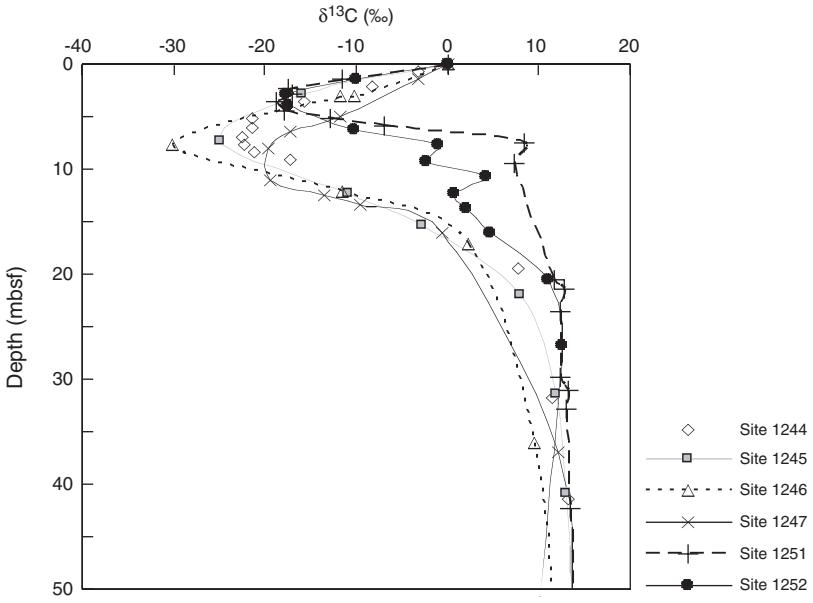

Figure F7. Plot of C_2–C_5 $\delta^{13}C$ hydrocarbon isomer vs. reciprocal of carbon number projected to C_1 axis provides an estimate of end-member thermogenic methane component in mixed biogenic-thermogenic gas (Chung et al., 1988).

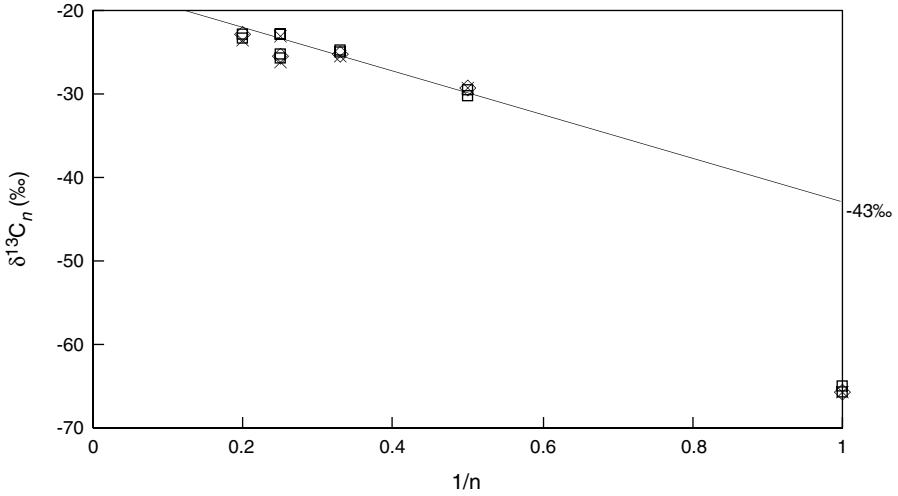

Figure F8. Porosity vs. depth and age vs. depth functions for Site 1244. At any given depth, pore water is older than containing sediment because of compaction and more rapid subsidence of sediment.

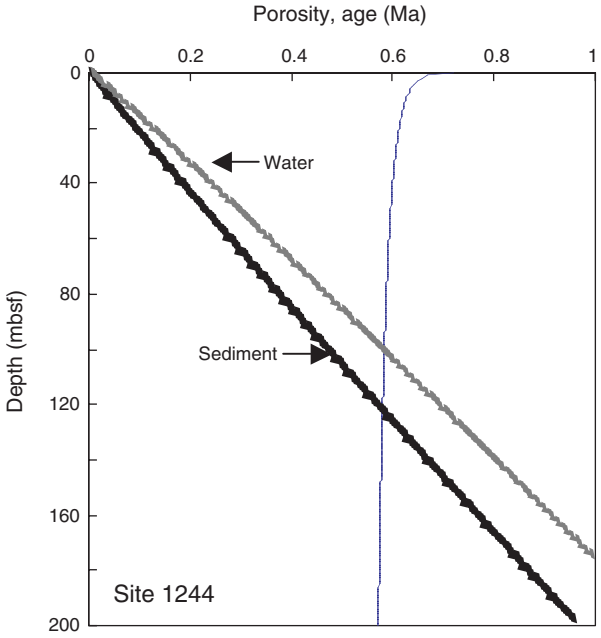

Figure F9. Dissolved sulfate concentration as a function of depth in sites away from the southern summit of Hydrate Ridge.

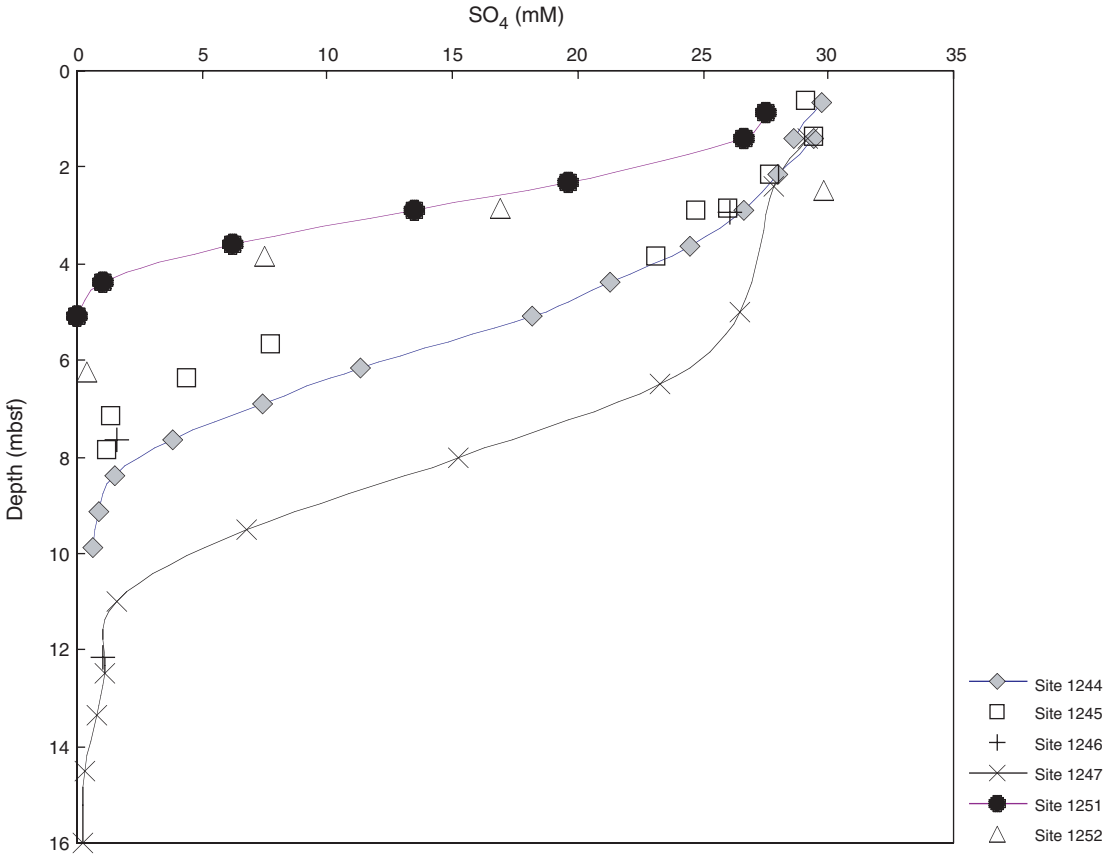

Figure F10. Sulfate reduction rate as a function of depth at Site 1244 estimated from diagenetic model with steady state assumptions and exponential curve fit of sulfate concentration profile.

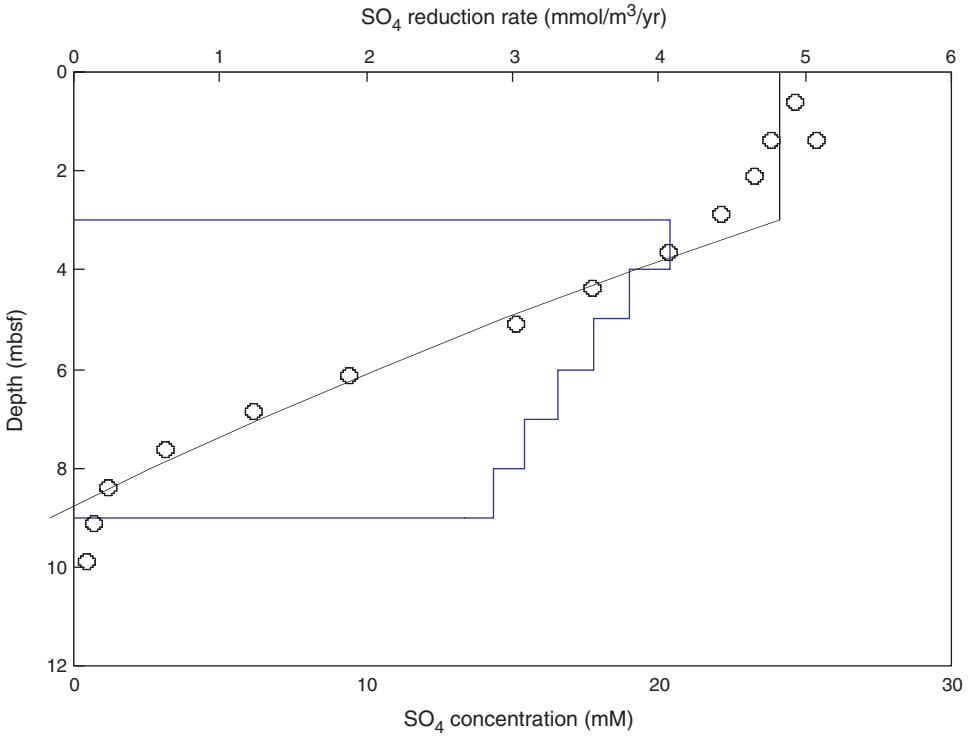

Figure F11. Plot of sulfate consumed vs. alkalinity produced, corrected for calcium and magnesium deficit, at Sites 1244, 1245, and 1247. Relationship is consistent with sulfate reduction fueled primarily by organic matter oxidation (slope 2:1) as opposed to anaerobic methane oxidation (slope 1:1).

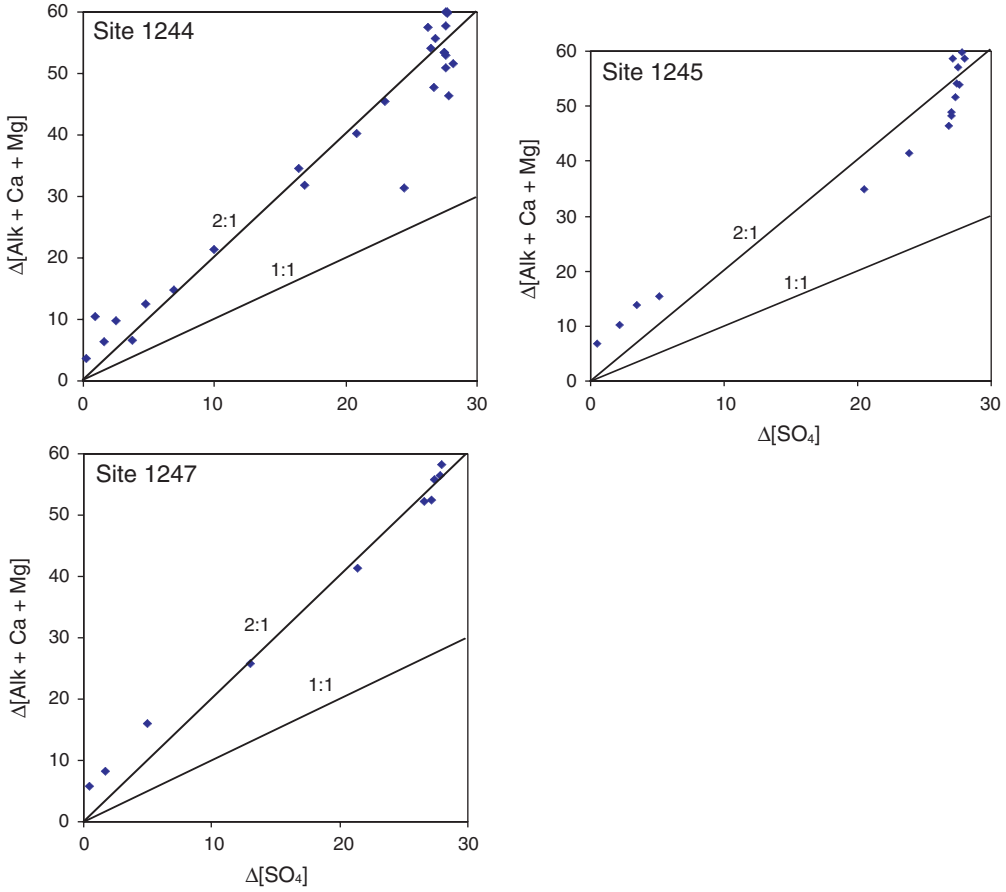

Figure F12. Concentration vs. depth profiles of alkalinity and methane at Site 1244. Also shown are methane concentration estimates from headspace methane (HS) and pressure core sampler (PCS) samples.

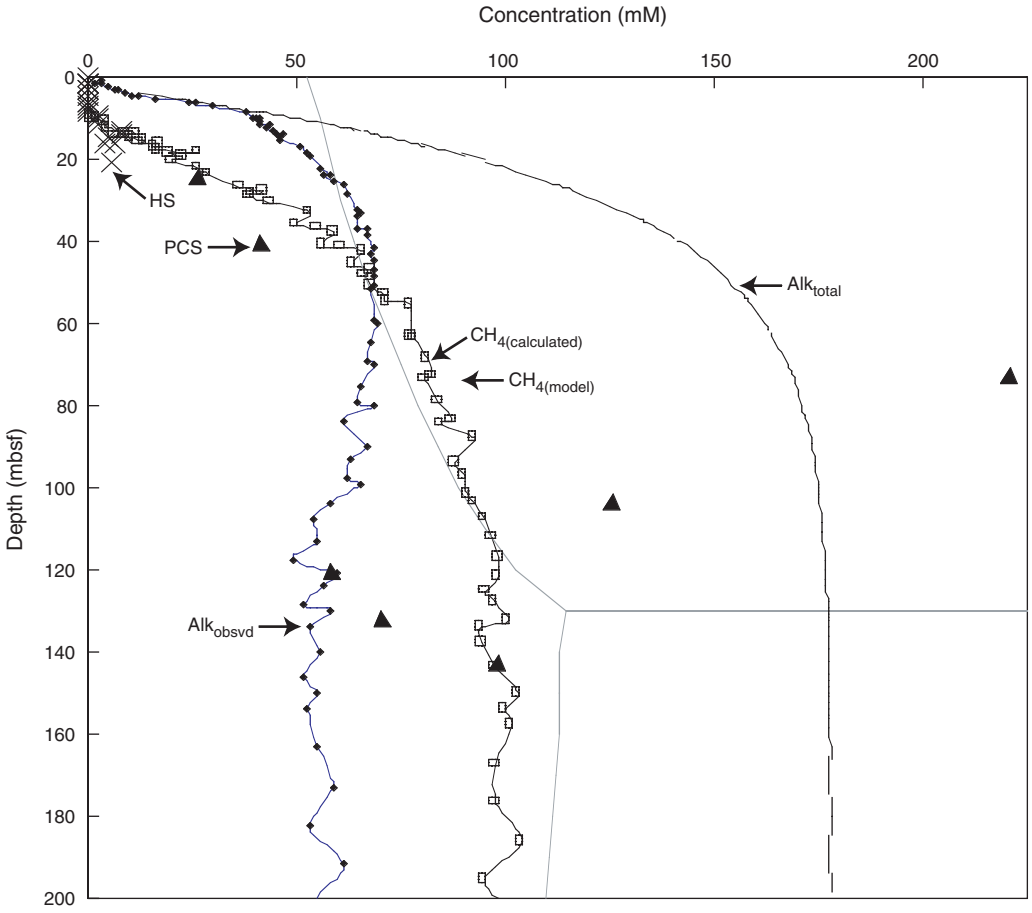

Figure F13. Methane production rate as a function of depth at Site 1244 estimated from steady state assumptions and exponential curve fit of alkalinity and methane concentration profiles.

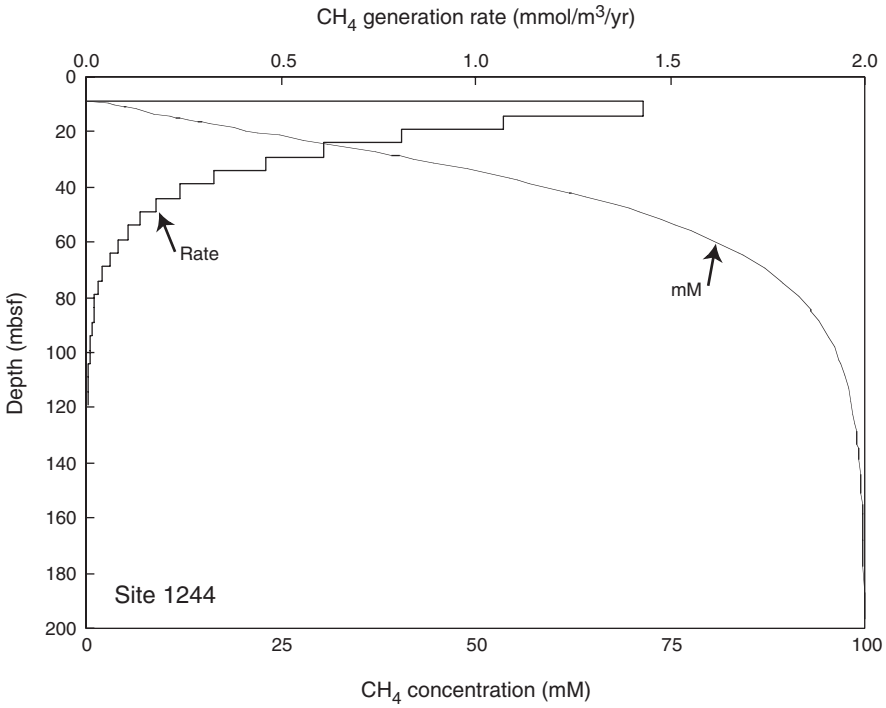

Figure F14. C_1/C_2 ratios of gas in DSDP/ODP cores showing dependence of ethane content on temperature history (heating rate). Thermal gradients are 200°C/km for Hole 1038, 70°C/km for Hole 229, and ~30°/km for Hole 1073. Bottom water temperature is 22°C at Site 229, and 2°–3°C at Sites 1038 and 1073. Sedimentation rates are 500–900 m/m.y. at each site.

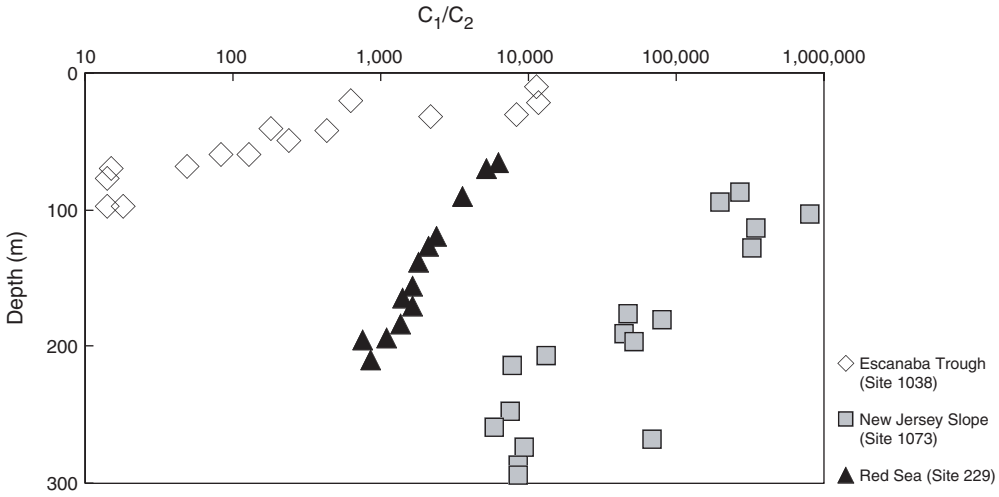

Figure F15. C_1/C_2 ratios of void gas samples as a function of depth at Sites 1252, 1244, and 1251. There is no offset in C_1/C_2 ratios of gas at the base of the hydrate stability zone (BHSZ) at Site 1252 because gas hydrates are absent or in low concentration. Significant offset at base of hydrate stability at Sites 1244 and 1251 are due to ethane fractionation during formation and decomposition of gas hydrates.

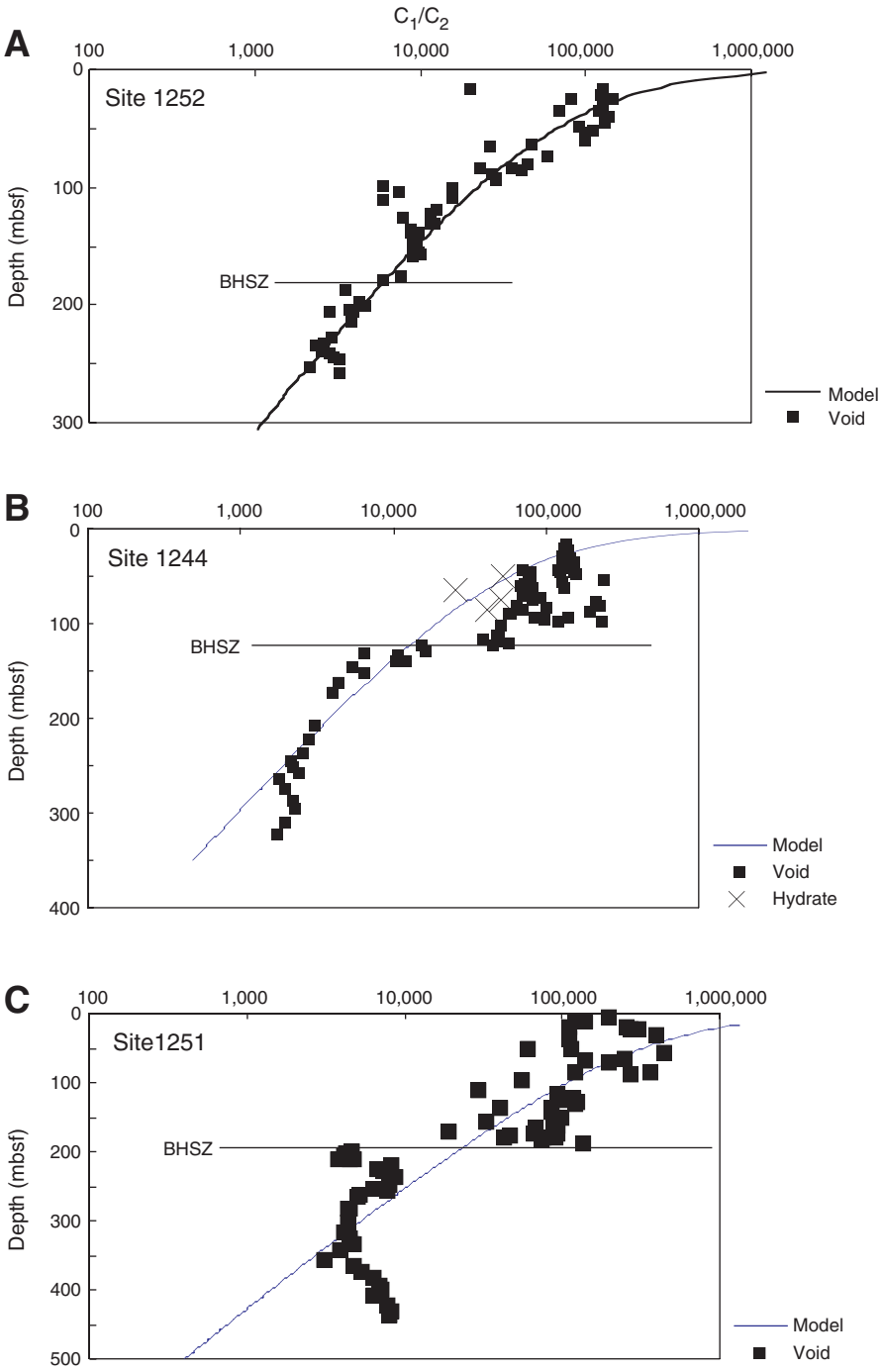

Figure F16. C_1/C_2 ratios of void gas samples from Eel River Basin (ODP Leg 169 Site 1019) shows offset at approximate depth of bottom simulating reflection and base of the gas hydrate stability zone (BHSZ).

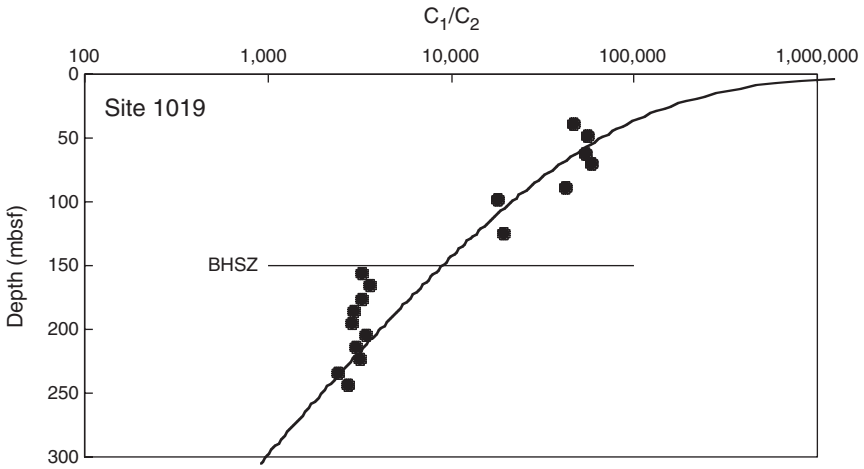

Table T1. Leg 204 site data.

Site	Latitude	Longitude	Water depth (mbsl)	BSR depth (mbsf)	Sediment accumulation rate (m/m.y.)	Depth interval (mbsf)
1244	44°35.17′N	125°7.19′W	895	128	270	0–80
1245	44°35.17′N	125°8.95′W	871	134	230	0–60
1246	44°35.16′N	125°8.13′W	850	121	310	0–85
1247	44°34.66′N	125°9.05′W	834	128	140	0–37
1248	44°34.45′N	125°9.15′W	830	115	210	2–50
1249	44°35.17′N	125°8.84′W	777	115	90	0–25
1250	44°35.17′N	125°9.01′W	796	114	90	0–25
1251	44°34.21′N	125°4.44′W	1210	193	630	0–170
1252	44°35.167′N	125°5.569′W	1040	170	280	0–90

Notes: Latitudes and longitudes are general locations of multiple holes, except Site 1252. Bottom-simulating reflector (BSR) depth for Site 1252 is projected from nearby seismic observations. Sediment accumulation rates are biostratigraphic estimates.

Table T2. Carbon isotopic composition of methane and carbon dioxide in void gas. (See table notes. Continued on next two pages.)

Core, section, interval, (cm)	Depth (mbsf)	C_1/C_2	$\delta^{13}C$ (‰ PDB)	
			C_1	CO_2
204-1244B-				
3H-1, 105	17.2	136,300	–73.7	–7.4
4H-2, 72	26.5	138,100	–72.1	0.2
4H-8, 33	35.1	144,500	–69.7	–0.3
5H-7, 101	44.1	71,100	–68.9	2.9
6H-3, 1	45.4	124,300	–67.9	2.5
6H-7, 60	52	79,300	–68.3	7.3
204-1244C-				
3H-1, 49	15.5	NA	–77.1	–7.7
4H-1, 110	25.5	NA	–69.2	1.4
5H-1, 121	35.2	142,900	–68.6	0.7
6H-2, 136	46.4	80,000	–68	1.3
7H-2, 122	54.7	77,600	–67.5	0.1
7H-3, 90	55.7	NA	–67.3	3.3
8H-7, 25.	70.7	69,800	–69.1	1.4
9H-2, 85	74.4	82,500	–67.2	3.4
10H-1, 61	82.1	64,100	–67.4	–0.9
12H-1, 107	101.6	50,500	–66.9	–0.8
13H-2, 69	112.1	47,600	–66.5	–1.1
15H-2, 35	122.9	15,400	–65.4	3.5
19X-3, 10	146.1	5,500	–60.5	–2.9
20X-3, 27	152.8	6,500	–64.6	0.3
21X-3, 88	162.7	4,400	–67.3	–2.2
22X-3, 90	172.2	4,000	–67.3	0.1
26X-2, 80	208.4	3,100	–66.7	–2.4
27X-5, 50	222.3	2,800	–65.1	1.7
29X-3, 37	237.6	2,600	–64.6	1.7
30X-1, 96	245.8	2,200	–65.5	–4
30X-5, 67	251.4	2,200	–64.1	0
31X-3, 150	258.8	2,500	–65.4	–2.4
32X-1, 75	264.8	1,800	–62.8	–0.4
33X-2, 2	275.1	2,000	–63.7	2.7
34X-4, 2	287.8	2,200	–63	3.4
35X-3, 2	296	2,300	–62.9	3.7
36X-7, 5	311.1	2,000	–62.3	0.6
38X-2, 14	323.5	1,800	–63.7	0.4
204-1244E-				
4H-1, 40	20.5	NA	–73.6	–5
4H-2, 68	22.4	133,900	–73.5	–1.9
5H-1, 113	30.8	132,900	–71.1	0.1
5H-7, 31	39	143,200	–69.6	2
7H-2, 103	43.7	121,500	–69.1	–0.1
7H-6, 101	49.7	59,300	–69.1	0.7
9H-4, 20	57	NA	–68.8	4.3
9H-5, 15	58.8	73,400	–68.2	0.2
10H-1, 36	62.5	133,500	–68.1	–0.5
12H-5, 68	80.3	226,700	–68.3	0.2
13H-1, 4	83.1	102,100	–64.1	2.1
13H-3, 2	86.2	70,200	–68.5	1.7
13H-5, 120	90.3	57,100	–67.3	2.2
14H-2, 3	94.1	84,800	–67.5	4
14H-4, 118	98.2	229,400	–64	0.7
17H-2, 108	116.2	38,800	–68.1	0.4
18H-1, 85	124	44,800	–68.1	–1.4
18H-6, 26	130.9	6,500	–67	1.1
204-1245B-				
3H-6, 46	27	165,800	–71.8	–2.6
7H-4, 78	61.6	48,550	–68.4	2
10H-1, 133	86.8	69,240	–67.7	4.1
11H-3, 97	98.4	90,160	–67.4	1.2
12H-5, 81	111.3	133,900	–66.9	2.2
14H-3, 50	126.1	3,070	–66.3	1
16X-2, 122	140.2	270	–64.1	2.3
18X-2, 25	150.6	360	–59.9	5.5
18X-4, 55	154	NA	–64.4	2.6
22X-4, 80	190.7	1,440	–63.2	–3.1
23X-1, 50	195.2	1,400	–64	0.5
26X-2, 91	226	6,330	–64.3	–0.2
29X-3, 16	255.8	9,230	–64.1	1.2
31X-2, 48	273.9	10,370	–64.1	–1.5
32X-2, 94	283.9	10,070	–63.6	–0.6
34X-6, 68	301.4	14,950	–63.9	–3.3
37X-4, 112	325.6	10,790	–64.4	–2
42X-2, 48	370	7,930	–64.5	–3
44X-1, 39	387.8	6,150	–64.8	–3.4
47X-4, 1	411.2	6,780	–65.5	–4.7
48X-3, 77	420.1	4,960	–65.9	–2
50X-4, 40	440.1	3,620	–65.8	–5.4
52X-3, 140	459.1	3,440	–66.4	–6.8
53X-5, 14	469.9	3,060	–65.7	–7.7
204-1245C-				
5H-1, 47	29	181,100	–66.9	5.5
7H-1, 126	48.8	44,450	–69.3	–3.9
10H-4, 100	73	53,100	–67.4	6.6
13H-4, 26	101.1	205,400	–67	2.8
14H-3, 70	110.2	40,560	–67.3	0.1
17X-2, 50	124	2,220	–65.9	2.2
19X-2, 12	131.6	200	–63.8	2.6
20X-3, 3	141.7	340	–64.4	2.7
21X-2, 131	151.2	250	–64.2	2.8
22X-5, 49	164.4	310	–63.1	5.3
23X-3, 70	171.1	340	–62.6	4.1
24H-6, 69	185.3	490	–61.2	4.6
25H-3, 63	190.2	840	–64.3	–0.2
26H-1, 135	192.5	1,140	–63.9	1.4
28H-1, 113	198	2,070	–63.3	3.7
204-1245D-				
3H-1, 12	14.6	15	–75.8	–11.6
3H-7, 51	24	17	–73.5	–2
204-1246B-				
3H-3, 20	17.4	109,000	–75.3	–5
4H-1, 97	24.7	104,300	–73.4	–5.1
5H-3, 62	36.8	75,100	–71.1	–2.8
6H-4, 71	47.8	52,800	–69.3	5.7
7H-3, 1	55	73,800	–70	3.5
8H-4, 5	66.3	44,500	–69.4	–2.7
9H-2, 1	72.4	61,700	–68.3	1
10H-1, 100	81.7	56,300	–68.5	0.9
11H-2, 33	92.5	93,500	–68.1	1.8
12H-2, 100	102.2	25,800	–67.4	2.5
13H-1, 150	110.7	2,680	–66.1	2.8
14H-2, 102	121.2	2,370	–66.8	0.9
15H-2, 1	123.8	1,930	–66.7	2.1
15H-5, 24	128.5	1,760	–65.4	1.2
16H-4, 73	135	1,490	–65.3	3.5
204-1247B-				
5H-1, 62	25.2	94,171	–73.1	–2.3
5H-2, 127	27.4	96,441	–71.6	–3.2
5H-7, 8	33.7	98,466	–70.4	0.8
6H-1, 119	35.3	94,299	–70.7	–1.3
6H-2, 71	37.8	90,729	–69.3	1.2
6H-7, 46	43.6	83,447	–70	0.2
7H-2, 88	46	78,301	–70.7	4.5
7H-4, 64	48.7	26,095	–70.9	6.3
8H-1, 71	53.8	73,269	–70.4	2.3
8H-2, 137	56	25,371	–70.7	5.2
8H-3, 138	57.4	44,737	–64.6	2.2
8H-4, 117	58.8	55,801	–68.9	0.5
9H-1, 95	63.5	70,735	–68.3	1.7
9H-3, 124	66.8	68,728	–69.6	2.2
10H-2, 46	74.1	47,542	–69.7	3.8
10H-4, 87	77.5	47,786	–67.8	4.4

Table T2 (continued).

Core, section, interval, (cm)	Depth (mbsf)	C_1/C_2	$\delta^{13}C$ (‰ PDB)	
			C_1	CO_2
10H-6, 58	80.2	49,731	–67.8	2.5
11H-1, 54	81.5	23,947	–65.4	3.8
11H-3, 13	84.7	26,160	–69.7	4.3
11H-6, 31	89.4	49,012	–67.4	1.8
12H-2, 1	92.6	23,815	–70	–0.5
12H-2, 50	93.1	24,626	–67.9	n.a.
12H-4, 1–27	96.9	49,558	–68.3	2.1
13H-2, 15	102.3	19,540	–68.4	2.1
13H-5, 11	106.7	31,025	–68	2.4
14H-1, 24	106.9	24,433	–67.5	0.8
14H-4, 105	112.3	32,632	–67.7	7.4
15X-2, 116	116.3	10,989	–68.7	–2.2
15X-3, 88	117.5	10,514	–62.9	2.9
19X-1, 129	135.9	844	–65	0.9
19X-3, 75	138.3	NA	–64.9	1.1
20X-1, 105	145.3	506	–65.8	1.3
20X-2, 115	146.9	473	–64.4	1.2
20X-3, 30	147.5	492	–65.3	1.7
20X-4, 88	149.6	446	–64.3	0.9
23X-1, 18	173.3	85	–65.8	–0.3
24X-4, 140	188.7	135	–65.6	1.8
24X-5, 140	190.2	142	–64.9	2.8
25X-3, 102	196.1	223	–65.7	0.9
25X-4, 118	197.5	230	–65	0
27X-1, 42	211.6	208	–63	0.4
204-1248B-				
2H-3, 50	9	492	–65.3	–2.9
204-1248C-				
1X-1, 100	1	740	–66.1	–18.4
3X-2, 150	22.3	1,033	–66.7	3.8
5X-1, 148	38.5	1,991	–68.8	1.1
6H-3, 99	50.8	3,201	–69.8	3.4
6H-5, 69	53	3,037	–68.3	7.6
6H-6, 120	55	2,920	–66.1	–1.5
7H-4, 20	62.2	4,759	–68.7	3.5
7H-6, 4	65	9,106	–68.6	3.4
8H-2, 15	68.7	5,974	–67.6	3.3
8H-5, 6	73	5,063	–65.8	0.8
9H-6, 99	85	5,139	–67.9	3.7
10H-5, 132	92.9	6,844	–66.8	2.9
11H-4, 70	99.8	5,495	–66	–0.2
11H-4, 70	99.8	5,557	–66.9	4.4
11H-6, 28	101.5	5,037	–66.9	2.6
12H-2, 98	107.5	2,262	–67.5	1.2
12H-3, 134	109.2	967	–65.7	4.4
13H-2, 7	116	793	–66.7	2.9
13H-4, 101	119.9	464	–66.4	2.9
14H-5, 101	129.8	166	–64.8	1.6
15H-1, 56	134.1	70	–64.4	2.1
16H-3, 107	140.6	136	–64.1	2
204-1249B-				
2A-1, 70	30.5	535	–67	–4.3
4A-1, 74	38.3	461	–68.2	–3
204-1249C-				
1H-1, 1	0.6	751	–66.6	–3.4
2H-1, 130	3.3	723	–65.2	–5
4H-5, 75	22	505	–64.9	–6.4
5H-3, 1	24.5	576	–64.5	–1.1
7H-6, 38	40.6	674	–65.6	3.8
8H-2, 24	46.2	1,503	–67.9	2.4
9H-3, 135	58.3	4,093	–68.6	–1.3
11H-5, 137	71	7,536	–67.9	3.7
12H-1, 110	76.2	14,602	–69.2	5.3
204-1249F-				
7H-3, 1	23.5	589	–60.3	–2.6
8H-2, 120	33	531	–65.8	–4.6
10H-2, 145	52.1	1,551	–64.6	–5.6
12H-2, 26	62.2	2,937	–68.6	–3.1
12H-5, 40	66.8	2,770	–69.1	1.8
15H-3, 22	75.4	5,340	–69.3	–0.6
15H-4, 64	77.4	6,372	–69	0.2
16H-3, 22	85.7	6,549	–68.6	3.6
204-1250B-				
1H-1, 100	1	1,268	–64.1	1.8
3H-1, 96	15	4,646	–64.7	2.5
3H-6, 145	23	7,434	–66.9	2.5
4H-4, 105	28.7	10,150	–67.5	1.3
5H-1, 120	34.2	9,414	–67.7	1.3
7H-5, 130	58	25,290	–67.2	4.6
8H-1, 120	62.7	45,155	–67.6	3.3
8H-6, 29	69.3	9,432	–69	2.5
10H-3, 6	75.5	7,709	–67.4	–2.1
10H-6, 33	80.3	12,163	–66.7	–0.9
12H-2, 66	93.3	12,702	–65.8	–0.8
13H-6,	107.9	2,434	–65.7	0.5
14H-1, 55	111.6	1,003	–63.4	4.5
17H-4, 20	133.7	2,156	–62.9	5
19H-4, 126	144.2	1,969	–62.9	5.1
204-1250D-				
4H-1, 149	27	16,379	–68.7	4.1
204-1250F-				
1H-2, 141	102.9	6,497	–67	1.6
1H-4, 7	104.6	2,456	–67.5	2.8
1H-4, 94	105.4	5,496	–66	1.1
1H-5, 75	106.8	1,820	–64	3.3
2H-3, 1	112.5	823	–67	5.3
2H-3, 7	112.6	827	–66.1	2.9
3X-2, 54	115.5	743	–65.4	2.4
5H-1, 34	121.3	1,230	–65	4.1
5H-1, 130	122	1,396	NA	3.7
6X-1, 100	128.3	1,443	–62.5	0.7
9X-2, 124	136.7	2,128	–62.1	1.6
11X-3, 145	157.7	223	–61.7	5.4
12X-1, 111	163.9	174	–62.1	4.8
12X-5, 45	169.3	179	–62.2	5.2
13X-2, 72	174.6	124	–61.9	3.7
13X-5, 30	178.7	126	–62.3	8.1
204-1251B-				
1H-4, 68	5.2	198,645	–74.7	–5.6
3H-3, 51	22	274,584	–71	1.5
4H-1, 57	28.7	NA	–67.3	2.3
4H-3, 20	31.3	399,181	–67.5	1.9
4H-7, 16	36.6	NA	–67.9	2.4
6H-2, 5	48		–68.1	2.6
7H-1, 149	58.1	442,341	–68.5	2.9
7H-6, 33	64.4	250,030	–68.5	3.6
8H-3, 82	69.9	140,672	–68.4	0.5
8H-4, 80	71.4	199,614	–67.9	3.5
10H-1, 150	86.6	368,417	–67.1	2.7
11H-2, 32	96.4	55,406	–67.6	3.3
13H-5, 37	111.9	29,370	–67.9	4
14H-3, 33	118.4	93,119	–67.1	3.6
15H-6, 14	132.7	120,307	–67.7	2.5
16H-6, 16	142.2	85,616	–65.4	2.7
17H-5, 105	151.1	88,374	–65.7	2
19H-6, 17	162.7	93,976	–67.5	3.4
20H-5, 142	170.6	18,931	–67.3	0.5
20H-2, 1	164.7	67,563	–66.1	3.7
22H-1, 93	173.6	66,788	–66	2.2
22H-5, 120	179.9	89,846	–62.3	
26X-2, 119	206.9	4,158	–64.5	0
27X-5, 35	219.9	8,394	–63.9	–1.5
28X-2, 41	225	6,732	–62.4	0.3
29X-3, 17	236	8,423	–64.6	0.2

Table T2 (continued).

Core, section, interval, (cm)	Depth (mbsf)	C_1/C_2	$\delta^{13}C$ (‰ PDB)	
			C_1	CO_2
29X-4, 13	237.4	8,879	–64	3.4
31X-4, 1	256.5	7,810	–62.2	3.7
32X-1, 106	262.8	5,216	–62.6	–0.7
34X-2, 102	283.5	4,415	–60	2.6
37X-3, 2	303.6	4,362	–61.5	2.2
38X-6, 5	317.7	4,196	–59.6	0.6
39X-3, 140	324.3	4,583	–60.2	5.8
41X-4, 5	335.2	4,685	–60.1	1.4
42X-2, 75	341.5	3,960	–60	2.4
43X-6, 82	357.1	3,126	–59.4	2.4
44X-6, 55	366.5	4,788	–59.3	2.9
45X-4, 100	373	5,436	–61.3	–0.5
46X-3, 100	381.6	6,301	–59.5	–0.6
47X-4, 124	393	7,000	–59.3	1.4
49X-2, 102	400.4	7,095	–58.3	2.2
50X-3, 5	409.6	6,360	–57	0.6
51X-5, 44	422.6	7,733	–60.9	3.6
52X-5, 98	432.8	8,393	–60.1	6.1
53X-2, 112	438.1	7,962	–59.6	0.2
204-1252B-				
3H-3, 31	16.5	128,853	–70.4	–0.9
4H-2, 25	25.7	81,088	–69.5	1.4
5H-2, 74	34.7	69,019	–69	3
5H-5, 90	39.4	138,490	–68.1	4.2
6H-4, 88	48.3	90,205	–67.8	5.9
7H-6, 44	60.3	98,206	–67	3.8
9H-7, 14	80.4	45,274	–66.7	0.5
11H-3, 1	93.4	28,792	–67.2	2.6
12H-3, 78	103.7	7,580	–66.7	1.4
13H-1, 130	110.7	6,061	–67.6	–0.2
14H-6, 1	126.1	7,844	–67.1	–1.8
15X-4, 72	130.1	12,341	–65.8	–3.3
16X-2, 1	136.2	8,912	–65.5	–0.3
17X-2, 1	145.9	9,692	–64.2	2.2
17X-5, 1	150.4	9,397	–66.2	1.3
18X-4, 1	158.6	8,977	–63.7	–0.1
20X-4, 53	178.5	6,011	–62.1	4.5
21X-4, 64	188.2	3,547	–60.1	3.6
23X-4, 20	206.2	2,870	–58.8	6.7
25X-6, 15	228.6	2,982	–56.8	1.8
26X-2, 42	232.4	2,615	–60.2	6.7
27X-2, 1	241.7	2,840	–62.1	2.7
27X-5, 25	246.4	3,298	–61.5	9.7
28X-6, 2	257.4	3,319	–62.9	3.9

Notes: PDB = Peedee belemnite. NA = not analyzed.

Table T3. Carbon isotopic composition of C_2–C_5 hydrocarbons in void gas.

Core, section, interval (cm)	Depth (mbsf)	$\delta^{13}C_2$ (‰)	$\delta^{13}C_3$ (‰)	$\delta^{13}C_{i\text{-}4}$ (‰)	$\delta^{13}C_{n\text{-}4}$ (‰)	$\delta^{13}C_{i\text{-}5}$ (‰)
204-1244B-						
27X-5, 50–51	222.30	–42.6				
33X-2, 1–2	275.05	–43.2				
36X-75, 6	311.09	–43.9				
204-1245B-						
7H-4, 78	61.62	–51.1				
10H-11, 33	86.83	–53.6				
18X-2, 25	150.63	–28.7	–24.9	–26.4	–23.8	
204-1245C-						
10H-4, 100	72.97	–52.5				
19X-2, 12	131.62	–29.2	–25.2	–26.7	–23.3	–23.3
22X-5, 49	164.39	–29.3	–25.0	–26.2	–22.2	–25.9
24H-6, 69	185.29	–29.1	–24.4	–25.8	–22.9	–25.8
204-1246B-						
15H-5, 24	128.49	–35.2	–27.0	–34.8		
204-1247B-						
15X-2, 116	116.26	–39.4	–26.2			
19X-3, 75	138.33	–33	–25.1			
20X-3, 30	147.50	–30.9	–26.0	–25.7	–23.1	
23X-1, 18	173.28	–29.4	–25.3	–25.4	–19.7	–22.9
24X-4, 140	188.70	–30.3	–25.1	–25.8	–22.9	–23.3
24X-5, 140	190.20	–29.6	–24.8	–25.3	–22.8	–22.9
25X-3, 102	196.05	–29.4	–25.4	–26.1	–23.1	–23.6
25X-4, 118	197.50	–29.5	–25.0	–26	–23.2	–23.5
27X-1, 42	211.63	–29.8	–25.3	–25.8	–23.3	–22.0
204-1248B-						
2H-2, 70–71	8.00	–31.5	–22.6	–33.2	–26.1	
2H-3, 50–51	9.00	–33.3	–24.5	–27.6	–28.3	
204-1248C-						
1X-1, 100–101	1.00	–35.1	–25.9			
5X-1, 148–149	38.48	–34.2	–24.7	–26.9	–24.1	
11H-6, 28–29	101.50	–35.1	–26.6	–27.7	–27.9	
14H-5, 101–102	129.76	–30.6	–26.6	–26.8	–22.7	–23.6
15H-1, 56–57	134.05	–30.6	–25.2	–25.6	–26.0	
16H-3, 107–108	140.57	–30.1	–25.6	–26.4	–24.5	
204-1250F-						
2H-3, 7	112.57	–37.8	–21.8			
3X-2, 54	115.54	–35.3	–23.3	–26.8		
5H-2, 55	123.05	–36.4	–19.6			
11X-3, 145	157.65	–31	–17.0	–26.6		
12X-1, 111	163.91	–31	–23.1	–26.5	–23.3	
13X-2, 72	174.62	–31.4	–26.0	–27.4	–24.0	–26.8
204-1251B-						
29X-3, 17-18	235.97	–42.5				
34X-2, 102-103	283.52	–38.8				
204-1252A-						
14H-6, 0	126.09	–43.2				
20X-2, 47	175.47	–35.4				
21X-4, 64	188.24	–34.5				
23X-4, 20	206.18	–32.9				
26X-2, 42	232.42	–36.8				
26X-6, 119	239.19	–41.8				
27X-2, 1	241.71	–41.8				
27X-5, 25	246.42	–36.5				
28X-3, 3	252.87	–41				
28X-6, 2	257.36	–40.9				

Table T4. Methane δD in void gas.

Core, section, interval (cm)	Depth (mbsf)	δD (‰)
204-1244B-		
6H-7, 60–62	52.03	–201
204-1244C-		
3H-1, 49	15.49	–193.5
4H-1, 110	25.50	–190.5
5H-1, 121–123	35.21	–184.2
8H-7, 25–26.	70.68	–200.9
10H-1, 61–63	82.11	–201.9
12H-1, 107–110	101.57	–201.0
13H-2, 69–71	112.09	–202.3
15H-2, 35–37	122.85	–198.4
20X-3, 27–28	152.77	–192.9
27X-5, 50–51	222.30	–189.2
33X-2, 1–2	275.05	–192.6
36X-7, 5–6	311.09	–190.9
38X-2, 14–15	323.54	–189.7
204-1244E-		
4H-1, 40	21.00	–207.5
9H-4, 20	57.00	–204.1
204-1245C-		
22X-5, 49	164.39	–195.5
204-1246B-		
3H-3, 20	17.40	–190.3
5H-3, 62	36.82	–191
7H-3, 1	55.00	–194.1
9H-2, 1	72.42	–195.8
12H-2, 100	102.20	–199.1
15H-5, 24	128.49	–195.3
16H-4, 73	135.03	–188.7
204-1247B-		
24X-5, 140	190.20	–190.8
204-1248C-		
6H-3, 99–100	50.76	–196.0
13H-2, 7–8	116.02	–185.4
15H-1, 56–57	134.05	–193.7
204-1250F-		
1H-4, 7	104.57	–195.6
13X-2, 72	174.62	–194.4
204-1251B-		
3H- 4, 102–103	24.03	–191.4
6H- 4, 101–102	51.83	–198.6
8H- 3, 82–83	69.92	–199.5
10H- 4, 87–88	88.00	–195.8
14H- 3, 33–34	118.44	–199.0
29X-3, 17–18	235.97	–191.6
34X-2, 102-103	283.52	–193.9
204-1252A-		
11H-7, 0	98.85	–203.8
13H-1, 130	110.70	–201.0
14H-6, 0	126.09	–188.2
20X-2, 47	175.47	–179.1
21X-4, 64	188.24	–177.3
23X-4, 20	206.18	–175.8
26X-2, 42	232.42	–185.9
26X-6, 119	239.19	–200.4
27X-2, 1	241.71	–192.3
27X-5, 25	246.42	–170.2
28X-3, 3	252.87	–188.2
28X-6, 2	257.36	–188.2

Table T5. Carbon isotopic composition of methane and carbon dioxide in PCS gas.

Core, section, interval (cm)	Depth (mbsf)	C_1/C_2	$\delta^{13}C$ (‰ PDB)	
			C_1	CO_2
204-1244C-				
14P	120.0		–64.5	
16P	131.0		–65.4	
16P-2	131.0		–66.4	
18P	142.0		–66.3	
18P-G2	142.0		–66.6	
204-1244F-				
4P-G1	23.6	117,374	–71.3	1.6
204-1244E-				
6P-G1	64.5		–68.9	
11P-G4	75.8		–68.1	
204-1245B-				
17P			–65.1	6.3
33P-G1	291.7	4,417	–65.1	–6.6
33P-G2	291.7	11,106	–65.6	
33P-G3	291.7	13,335	–66.1	–7.3
33P-G4	291.7	11,982	–63.2	
33P-G5	291.7	10,983	–65.1	–3.2
33P-G6	291.7	10,804	–65.5	0.7
204-1245C-				
3P-G1 total	17.5	48,785	–75.1	
8P-G1	57.5	73,546	–68.7	
8P-G2	57.5	179,625	–68.8	
8P-G3	57.5	5,879	–66.7	
8P-G4	57.5	147,119	–66.5	
8P-G5	57.5	143,493	–68.5	–3.1
8P-G6	57.5	55,635	–67.5	–3.5
8P-G7	57.5	114,987	–67.6	–3.9
8P-G8	57.5	105,301	–68.1	–3.4
16P-G3	120.5	4,211	–67.6	
16P-G4	120.5	4,179	–66.8	
16P-G5	120.5	4,055	–67.9	
16P-G10	120.5	3,645	–67.6	
16P-G15	120.5	3,473	–66.1	
16P-G20	120.5	3,060	–67.6	
16P-G25	120.5	3,127	–68.2	–2.2
16P-G30	120.5	2,580	–67.8	2.0
204-1247B-				
4P-G1	23.1	460,317	–72.2	
16P-G1	123.8	60,728	–67.9	
16P-G4	123.8	3,866	–68.3	
16P-G5	123.8	2,504	–67.7	
16P-G8	123.8	2,381	–67.5	
16P-G12	123.8	2,666	–66.4	
16P-G15	123.8	2,515	–67.2	
16P-G16	123.8	2,083	–67.3	–5.4
204-1249C-				
6P-G7	34.0	616	–65.1	
6P-G11	34.0	645	–65.3	0.1
6P-G17	34.0	636	–64.7	2.4
204-1249F-				
4P-G1	14.0	664	–71.8	1.6
4P-G2	14.0	1,026	–65.8	–11
4P-G3	14.0	1,006	–65.2	
4P-G6	14.0	951	–60.4	–13.7
4P-G7	14.0	1,100	–65.5	–4.1
4P-G8	14.0	1,317	–65.5	–8.1
4P-G9	14.0	1,394	–65.4	
4P-G10	14.0	1,252	–65.5	–12.1
4P-G11	14.0	984	–65.4	
4P-G13	14.0	753	–66	
4P-G14	14.0	786	–65.1	
4P-G18	14.0	783	–65.4	–18.1
4P-G22	14.0	689	–65.9	–3.1
4P-G28	14.0	746	–65.6	–3.1
4P-G35	14.0	663	–67	
4P-G49	14.0	679	–65.4	
4P-G68	14.0	725	–65.3	–8.4
4P-G71	14.0	661	–65.5	1.6
4P-G82	14.0	619	–65.8	–8
4P-G96	14.0	555	–65.6	–3.4
204-1250D-				
5P-G1	35.5	18,050	–70.3	
5P-G2	35.5	16,571	–69.1	
5P-G3	35.5	14,995	–68.8	
5P-G4	35.5	16,483	–69	
204-1250F-				
4P-G4	119.5	917	945	–66.5
204-1251B-				
12P-G3	104.6	58,968	–68.5	1.7
18P-G3	154.1	86,669	–68	3.0
35P-G4	291.1	4,755	–62.2	
204-1251D-				
6P-G4	46.4	119,668	–70.2	
10P	69.4		–69.2	–2
21P-G3	173.9		–67.1	
29P-G5	228.0	7,949	–65.4	
204-1251G-				
2P-G4	20.5	180,577	–71.1	–7.3

Note: PDB = Peedee belemnite.

Table T6. Carbon isotopic composition of methane and carbon dioxide in hydrate-bound gas.

Core, section, interval, (cm)	Depth (mbsf)	C_1/C_2	$\delta^{13}C$ (‰ PDB)	
			C_1	CO_2
204-1244C-				
8H-1, 47–52	65.0	25,647	–67.1	–13.5
10H-2, 70–103	85.0	40,934	–69.5	–5.1
204-1244E-				
12H-1, 60–6X	74.2	50,583	–68.3	1.6
204-1245B-				
6H-5, 103	54.5	60,730	–69.1	–1.3
9H-CC	85.0	45,431	–67.5	1.7
204-1245C-				
13H-4, 56–76	101.4	47,463	–67.8	–3.3
204-1246C-				
12H-4	105.1	53,957	–68.2	–9.7
204-1247B-				
12H-2, 41–51	93.0	24,150	–70	–3.9
204-1248B-				
1H-1, 50–55	0.5	726	–68.1	–30
1H-HYD 2	2.0		–67.1	–11.7
1H-CC	2.2	625	–67.2	–3.5
2H-2, 0–25	7.4	279	–66.2	2
204-1248C-				
1X-2, 0–10	1.5	739	–65.9	–26.1
1X-CC	2.2	563	–66.1	–2.6
3X-CC	22.4	753	–67	1.9
8H-6, 85–87	74.6	2,994	–66.3	2.5
10H-1, 100–119	87.0	2,017	–67.8	0.2
204-1249B-				
4A-1, 74–82	38.3	284	–64.8	–3.8
204-1249C-				
1H-1, 105–120	1.1	1,124	–66.2	–0.1
1H-1, 195–200	2.0	824	–65.3	
2H-1, 0–5	2.0	492	–63.3	–9.9
2H-CC	5.0		–66.4	–12.3
3H-1, 106–131	6.1	594	–67	–2
4H-2, 62–72	18.0	563	–66	–2
4H-3, 57–59	19.6	272	–65.4	2.3
204-1249D-				
1H-CC	2.1	640	–68	–6.7
3H-1, 150–160	10.5	699	–66.8	3.7
204-1249E-				
1H-1, 0–10	0.0	746	–68	–4.8
3H-2, 70–80	10.3	993	–65.3	5.1
204-1249F-				
1H-1, 0–20	0.0	898	–68	
1H-mbio	2.0		–67.2	–11.9
5H-1, 64–70	16.1	602	–63.2	
5H, bottom	16.3		–63.2	2.5
6X-1, 100–110	17.6	352	–64.2	–16.7
6X-1, bottom	17.7		–64.6	–3.4
8H-2, 102–112	32.9		–66.4	1.4
8H-2, 117–127	33.0	431	–63.5	1.4
204-1250C-				
1H-CC	1.4	1,163	–66	–5.4
2H-CC	6.5	1,513	–64.8	6.7
11H-3, 120	86.7	22,742	–67.4	–3.6
12H-1, 50	92.5		–66.8	–12.7
204-1250D-				
1H-1?	1.0	1,329	–65.5	–18.3
1H-2, 14–17	1.6	1,156	–65.6	3.5
10H-3, 53–84	81.5	45,456	–69.4	1.1
204-1250F-				
1H-1, 23	100.2	33,981	–70.2	0.5

Notes: PDB = Peedee belemnite. Blank = no analysis.

Table T7. Carbon isotope composition of dissolved inorganic carbon.

Core, section	Depth (mbsf)	$\delta^{13}C$ (‰)
204-1244C-		
1H-1	0.65	–3.2
1H-2	2.15	–8.3
1H-3	3.65	–15.7
1H-4	5.10	–21.4
2H-1	6.15	–21.5
2H-1	6.90	–22.5
2H-2	7.65	–22.3
2H-2	8.40	–21.3
2H-3	9.15	–17.2
3H-3	19.40	7.7
4H-5	31.85	11.4
5H-5	41.35	13.2
7H-2	54.79	14.7
7H-5	58.97	14.6
9H-2	74.85	13.6
10H-2	83.55	13.8
12H-2	103.35	12.6
13H-2	112.85	12.8
13H-5	117.35	11.7
15H-2	123.85	12.7
17H-2	133.70	12.6
19X-5	148.85	13.6
21X-3	163.15	13.1
23X-3	182.25	13.9
26X-3	210.10	13.7
27X-3	220.10	13.2
29X-3	238.56	14.7
31X-3	258.65	14.2
34X-3	287.60	13.4
39X-1	332.80	15.3
204-1245B-		
1H-2	2.90	–15.9
1H-5	7.40	–24.9
2H-2	12.40	–10.9
2H-4	15.40	–2.7
3H-2	21.90	8.0
4H-2	31.40	12.0
5H-2	40.90	12.9
6H-2	50.40	13.6
6H-5	54.28	14.0
7H-2	58.95	13.7
8H-2	64.99	13.6
9H-2	78.66	13.5
10H-5	92.53	13.4
11H-5	101.87	13.3
13H-5	120.80	12.8
15X-3	130.66	13.5
16X-3	141.80	13.7
19X-2	159.75	13.8
20X-2	169.25	14.5
21X-2	178.77	13.5
21X-4	181.27	13.6
22X-5	192.65	13.5
23X-5	201.95	13.2
25X-2	216.74	12.9
27X-2	236.05	11.8
29X-2	255.35	11.1
31X-5	278.76	9.3
34X-2	295.95	8.9
36X-2	313.15	9.2
38X-5	336.95	8.9
40X-2	351.65	9.2
41X-2	361.25	10.2
43X-4	383.55	8.7
45X-2	399.85	8.3
49X-4	430.11	7.5
51X-2	447.95	6.4
53X-2	466.51	6.3
204-1245E-		
2R-1	482.29	4.10
4R-1	502.20	5.10
204-1246B-		
1H-2	2.95	–10.1
1H-2	2.95	–11.7
2H-2	7.65	–30.2
2H-5	12.15	–11.6
3H-2	17.10	2.40
5H-2	36.10	9.50
7H-2	54.89	11.7
9H-2	73.81	13.5
11H-2	93.10	14.2
13H-2	112.05	14.0
16H-2	132.70	14.3
204-1247B-		
1H-1	1.40	–3.3
2H-1	5.00	–11.9
2H-2	6.50	–17.2
2H-3	8.00	–19.6
2H-5	11.00	–19.4
2H-6	12.50	–13.5
2H-7	13.37	–9.6
3H-2	16.00	–0.5
6H-2	37.00	12.1
8H-2	56.00	13.6
10H-5	79.50	13.3
12H-5	97.51	12.0
15X-2	116.45	14.4
19X-2	137.37	13.2
21X-3	158.20	14.3
25X-3	196.33	12.1
27X-3	215.50	10.8
204-1248B-		
1H-1	0	–19.2
1H-2	1.2	–0.9
2H-1	7.27	17.6
2H-3	9.16	18
204-1248C-		
1X-1	1.38	–23.6
2X-CC	10.68	15.6
3X-1	20.6	16.3
5X-1	39.80	14.40
5X-CC	41.18	15.20
7H-2	60.40	14.40
9H-2	79.40	13.80
11H-4	100.36	14.30
12H-2	107.81	14.00
13H-2	117.33	14.40
13H-4	120.21	14.50
17X-3	146.35	14.00
204-1249C-		
2H-2	3.55	13.11
3H-1	5.74	17.07
3H-2	6.96	16.33
4H-5	17.61	12.91
5H-2	25.70	14.04
7H-1	35.71	15.01
8H-3	47.64	14.94
9H-2	56.83	14.14
8H-3	69.17	13.60
13H-2	86.29	14.00
204-1249F-		
9H-3	43.61	12.87
10H-2	52.09	12.73
12H-2	63.20	12.73
15H-5	79.57	12.60
16H-4	88.50	12.64
204-1250C-		
1H-1	0.00	14.1
3H-5	21.40	14.6
4H-4	29.00	14.0
5H-5	40.31	13.6
6H-2	44.57	14.4
7H-5	58.00	13.3
10H-5	79.80	14.7
11H-3	86.36	14.4
12H-5	98.43	14.9
14H-2	113.80	15.1
15H-1	121.56	15.5
19X-5	145.75	16.6
5H-1	122.30	15.3
10X-3	147.90	16.7
11X-2	155.68	16.6
13X-3	176.65	15.7
204-1251B-		
1H-2	2.95	–0.5
1H-5	7.45	8.30
3H-2	21.43	12.7
4H-2	31.00	13.2
6H-5	53.61	13.8
11H-5	100.74	14.0
23H-4	187.72	13.5
26X-2	205.83	13.4
28X-2	225.85	13.7
30X-4	248.00	13.3
32X-2	264.45	13.2
34X-2	283.78	6.7
36X-5	299.40	6.80
38X-3	314.60	7.1
39X-3	324.20	13.7
41X-2	333.40	13.1
43X-2	350.43	7.3
45X-3	372.30	7.4
47X-3	391.60	13.7
49X-3	402.20	15.9
51X-3	402.50	16.50
53X-3	439.78	18.4
204-1251D-		
1X-2	2.40	-17.4
2X-1	9.50	7.3
3X-2	20.50	11.6
3X-4	23.50	12.3
4H-2	29.80	12.3
4H-2	32.80	12.9
5H-5	42.40	13.5
7H-3	52.07	13.9
8H-5	64.75	13.0
11H-4	82.29	13.4
11H-4	83.64	13.5
13H-6	103.67	13.7
15H-5	122.40	13.2
17H-5	141.40	12.7
19H-2	156.31	12.9
19H-5	160.81	12.5
20H-2	166.13	12.8
20H-5	170.63	12.5
22X-1	175.60	12.4
22X-2	176.87	12.40
23X-2	181.82	12.7
23X-3	183.32	12.6
24X-2	189.62	12.4
24X-3	191.12	11.7
24X-3	192.52	12.1
24X-4	193.05	12.4
25X-2	200.95	12.4
25X-2	205.45	12.2
26X-3	210.38	13.1
204-1251E-		
1H-1	0.85	–17.3
1H-1	1.40	–11.5
1H-2	2.90	–17
1H-3	3.60	–18.8
1H-3	4.40	–17.8
1H-4	5.10	–12.9
1H-4	5.90	–6.9
204-1252A-		
1H-1	1.35	–9.9
1H-2	2.85	–17.7
1H-3	3.85	–17.4
2H-1	6.25	–10.3
2H-2	7.25	–1.1
2H-3	9.25	–2.3
2H-4	10.75	4.3
2H-5	12.25	0.8
2H-6	13.75	2.0
3H-2	16.00	4.6
3H-5	20.50	11.1
4H-2	26.75	12.5
8H-2	64.75	8.6
10H-2	82.85	8.2
12H-2	102.75	6.8
14H-2	121.75	9.6
16X-4	140.50	10.7
20X-3	177.80	14.7
22X-3	197.00	14.3
24X-3	215.50	14.2
26X-3	234.80	–2.1

Table T8. BSR temperatures and depths.

Site	Reflector	Water depth (mbsl)	Seismic depth (mbsf)	Estimated pressure (Mpa)	Estimated temperature (°C)	Hydrate temperature (°C)	Depth (mbsf)	Hydrate structure
1245		871						
	BSR1		131	10.16	12	12.07	132	I
	BSR2		158	10.43	13.56	13.65	159	II
1247		834						
	BSR1		130	9.79	11.94	11.73	125	I
	BSR2		152	10.02	13.22	13.36	153	II
1248		830						
	BSR1		119	9.63	11.4	11.58	122	I
	BSR2		145	9.9	12.91	13.28	151	II

Notes: Estimated pressure calculated as total depth (water + sediment; m) × 0.01015 MPa/m. Estimated temperature calculated as sediment depth (m) × 0.058°C/m + 4.4°C. Hydrate temperature calculated from CSMHYD (Sloan, 1998) using gas composition, pressure, and 3.5% NaCl salinity. Depth for hydrate temperature calculated using temperature from CSMHYD and depth (m) = (T – 4.4°C)/0.058°C/m. Hydrate structure determined by calculations from CSMHYD (Sloan, 1998).

Table T9. Sulfate reduction rate parameters.

Site	C_∞ (mM)	k/ω (1/m)	Burial velocity (m/m.y.)	Integrated rate (mmol/m²/yr)		G_o (mmol/g)	Carbon required (wt%)
				Linear	Exponential		
1244	–80	0.057	270	24	19	0.28	0.34
1245	–92	0.069	230	33	20	0.35	0.42
1246	–80	0.057	310	26	17	0.26	0.31
1247	–75	0.052	140	21	14	0.4	0.48
1251	–105	0.085	630	50	29	0.23	0.27
1252	–105	0.085	280	41	20	0.35	0.42

Notes: Parameters estimated from pore water sulfate gradients. G_o = metabolizable organic matter.

Table T10. Methane production rate parameters.

Site	C_∞ (mM)	k/ω (1/m)	Burial velocity (m/m.y.)	Integrated rate (mmol/m²/yr)	G_o (mmol/g)	Carbon required (wt%)
1244	160	0.057	270	39	0.26	0.31
1245	184	0.069	230	46	0.36	0.44
1246	160	0.057	310	34	0.24	0.28
1247	150	0.052	140	26	0.34	0.41
1251	210	0.085	630	81	0.27	0.32
1252	210	0.085	280	75	0.42	0.5

Notes: Parameters estimated from alkalinity mass balance. G_o = metabolizable organic matter.